Electronic Supplementary Material (ESI) for ChemComm.

Supporting Information

The Effect of Axial and Helical Chirality on Circularly Polarized Luminescence. Lessons Learned from Tethered Twistacenes.

Anjan Bedi,*[‖†a] Gal Schwartz,[‖b] Uri Hannanel,[b] Amit Manor Armon,[a] Israa Shioukhi,[a] Gil Markovich[b] and Ori Gidron*[a]

[a]*Institute of Chemistry, Center for Nanoscience and Nanotechnology and the Cazalli Institute, The Hebrew University of Jerusalem, Jerusalem 9190401, Israel. E-mail: ori.gidron@mail.huji.ac.il.*

[b]*School of Chemistry, Raymond and Beverly Sackler Faculty of Exact Sciences, Tel Aviv University, Tel Aviv 6997801, Israel. Email: gilmar@post.tau.ac.il.*

† Present address: Department of Chemistry, SRM Institute of Science and Technology, Kattankulathur, 603203, Tamil Nadu, India.

‖ These authors contributed equally.

Table of Contents

S1 General

Enantiopure compounds **5-Cn** were synthesized according to a previous report.[1] Flash chromatography (FC) was performed using CombiFlash SiO_2 columns with hexane/dichloromethane as eluent. ^{1}H and ^{13}C NMR spectra were recorded in solution on a Bruker-AVIII 500 MHz spectrometer using tetramethylsilane (TMS) as the external standard and chloroform-d as the solvent. Chemical shifts are expressed in δ units. UV-vis absorption spectra were recorded with an Agilent Cary-5000 spectrophotometer. The spectra were measured using a quartz cuvette (1 cm) at 25 °C. The absorption wavelengths are reported in nm with the extinction coefficient ε ($M^{-1}cm^{-1}$) in brackets. Steady state fluorescence measurements were performed on a HORIBA JOBIN YVON Fluoromax-4 spectrofluorometer with the excitation/emission geometry at right angles. Fluorescence quantum yields (ϕ_f) were determined using a standard procedure under a HORIBA-Φ integrating sphere. Electronic Circular Dichroism (ECD) spectra were recorded on a MOS-500 spectrophotometer from BioLogic Science Instruments.

For electrochemical measurements, dichloromethane (DCM) containing 0.1 M tetrabutylammonium hexafluorophosphate ($TBAPF_6$) was used as a solvent. Ag/AgCl was used as a reference electrode by dipping a silver wire in an aqueous solution of $FeCl_3$ and HCl. Platinum-disk and platinum-wire electrodes were applied as working and counter electrodes, respectively. All electrochemical measurements were performed under a dry nitrogen atmosphere. Anhydrous DCM was purchased from Sigma-Aldrich and used as received.

High resolution mass spectra were analyzed on an Agilent HR Q-TOF-MS mass spectrometer using the dual-ESI technique operating in the positive mode. MALDI-TOFMS spectra were acquired using an MALDI-TOF/TOF autoflex speed mass spectrometer (Bruker Daltonilk GmbH, Bremen, Germany) equipped with a smartbeam-II solid-state laser (modified Nd:YAG laser) λ = 355 nm. The instrument was operated in positive ion, reflectron mode. The accelerating voltage was 21.0 kV. The delay time was 130 ns. Laser fluence were optimized for each sample. The laser was fired at a frequency of 2 kHz and spectra were accumulated in multiples of 500 laser shots to achieve 1500 shots in total. Sample preparation: 2-[(2E)-3-(4-tert-butylphenyl)-2-methylprop2-enylidene]malononitrile (DCTB) matrix solutions were prepared to a concentration of 20 mg/mL in DCM. Sample solutions were made to an approximate concentration of 5 mg/mL in DCM. Sample and matrix solutions were premixed at a ratio of 1:10 or 1:40 (v/v). A volume of 0.5 μL of

this mixture was placed on a MALDI steel target plate. After evaporation of the solvent, the target was inserted into the mass spectrometer.

Sample preparation for CPL measurements

All compounds were freshly prepared before each measurement and dissolved in nitrogen purged $CHCl_3$.

Experimental setup for CPL measurements

All measurements were performed in a home-built CPL system using a photoelastic modulator and lock-in detection.[2] The samples were excited using a 395 nm diode laser (Vortran Stradus, 100 mW). Light emitted from the samples was collected at 90° to the excitation, passed through the monochromator, and detected by a photomultiplier. The laser light passed through a shortpass filter with a cutoff wavelength of 450 nm and the emitted light passed through a longpass filter with a cutoff wavelength of 450 nm at the entrance to the monochromator in the measurements of samples C4, C6 (C3 was measured without the longpass filter). A fused silica cuvette of 1 cm optical path length was used for all measurements.

S2 Synthesis of 4-Cn

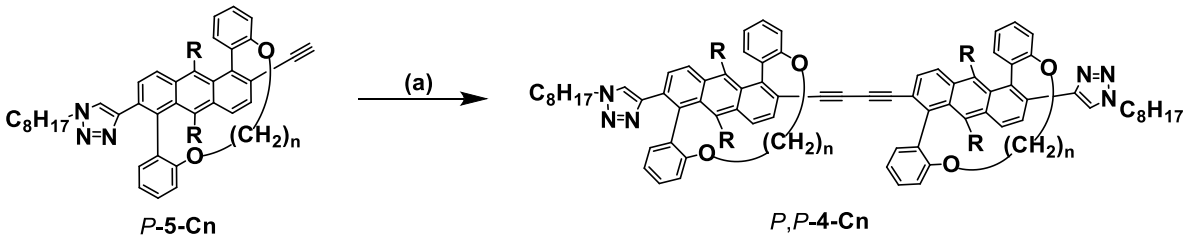

Scheme S1. Synthesis of *P,P*-**4-Cn** from *P*-**5-Cn.** Step (a): $Pd(PPh_3)_4$, THF/Et_3N (1/1), RT, 4 h.

General method for synthesis of *P,P*-4-Cn (n=4, 6, or 8 methyl groups)

Synthesis of P,P-4-C8

To a single necked round-bottomed (RB) flask kept under Ar flow was added *P*-**5-C8** (10 mg, 0.012 mmol), tetrakis(triphenylphosphine)palladium(0) ($Pd(PPh_3)_4$; 1.38 mg, 0.0012 mmol) and CuI (0.45 mg, 0.0024 mmol). Triethylamine/tetrahydrofuran (Et_3N/THF; 2 mL/2mL) was purged with Ar for 5 min and then added to the previously mixed reagents and the reaction mixture was

stirred for 4 h at room temperature (RT) until complete consumption of *P*-**5-C8** was observed by thin-layer chromatograph (TLC). The solvent was evaporated and the reaction mixture was loaded directly onto a silica gel column and eluted with ethyl acetate/hexane (1/5) to afford *P*-**4-C8** as a yellow solid (9.6 mg, yield = 96%) with green emission under a 365 nm lamp.

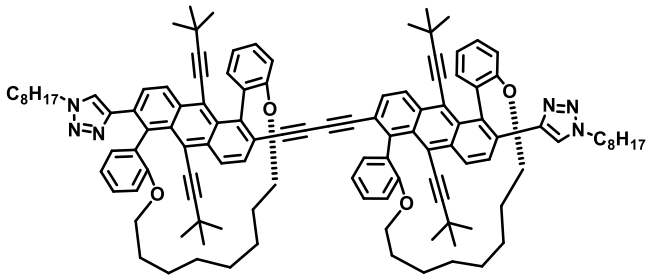

^{1}H NMR (500 MHz, $CDCl_3$) δ 8.80 (d, *J* = 9.4 Hz, 2H), 8.61 (d, *J* = 9.2 Hz, 2H), 8.46 (d, *J* = 9.4 Hz, 2H), 7.53 – 7.43 (m, 6H), 7.40 (dd, *J* = 7.4, 1.7 Hz, 2H), 7.20 (dd, *J* = 7.4, 1.7 Hz, 2H), 7.08 (td, *J* = 7.4, 0.9 Hz, 2H), 7.02 (td, *J* = 7.4, 0.9 Hz, 2H), 6.96 – 6.90 (m, 2H), 5.74 (s, 1H),
4.15 – 4.06 (m, 4H), 3.95 (dt, *J* = 8.6, 4.3 Hz, 2H), 3.84 – 3.73 (m, 6H), 1.70 (m, 4H), 1.27 (s, 28H), 1.14 (s, 36H), 0.91 (t, *J* = 7.0 Hz, 6H), 0.71 – 0.39 (m, 16H).

^{13}C NMR (126 MHz, $CDCl_3$) δ 158.4, 157.6, 146.7, 142.5, 133.8, 134.7, 133.5, 132.7, 132.0, 131.6, 130.7, 130.1, 129.9, 129.5, 129.37, 129.35, 128.5, 128.0, 127.4, 126.8, 121.94, 121.91, 121.1, 120.2, 120.0, 119.3, 116.0, 115.9, 112.3, 111.8, 83.3, 79.2, 78.9, 78.8, 69.4, 69.0, 49.8, 31.7, 30.9, 29.9, 29.8, 29.5, 29.3, 29.0, 28.9, 28.9, 28.5, 27.1, 26.7, 26.3, 22.64, 22.62, 14.09, 14.06.

MS (MALDI-TOF, m/z): calcd for $C_{116}H_{128}N_6O_4$, 1670.002; found 1670.011.

UV-vis ($CHCl_3$): λ_{max} (ε) = 277 (197730), 327 (184342), 370 (80489), 390 (92382), 423 (52880), 451 (64582), 481 nm (67677 M^{-1} cm^{-1}).

*Synthesis of P,P-**4-C6***

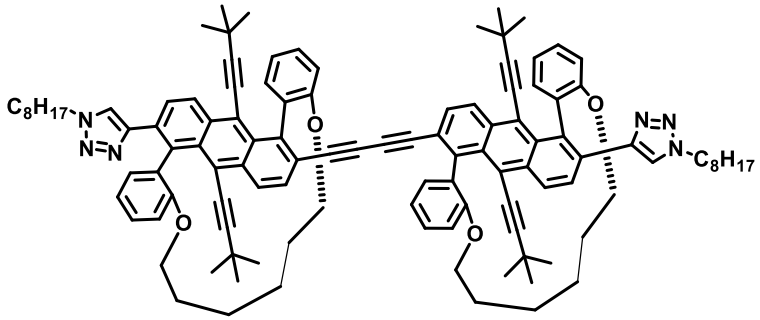

Reaction of *P*-**5-C6** (10 mg, 0.012 mmol), $Pd(PPh_3)_4$ (1.38 mg, 0.0012 mmol) and CuI (0.45 mg, 0.0024 mmol) and triethylamine/THF (1.5ml/2.5mL) furnished *P*,*P*-**4-C6** (9.6 mg, yield = 96%) as a yellow solid with green emission under a 365 nm lamp.

^{1}H NMR (500 MHz, $CDCl_3$) δ 8.74 (d, *J* = 9.3 Hz, 2H), 8.55 (d, *J* = 9.2 Hz, 2H), 8.44 (d, *J* = 9.3 Hz, 2H), 7.70 (dd, *J* = 7.5, 1.7 Hz, 2H), 7.52 (d, *J* = 9.2 Hz, 2H), 7.47 (m, 4H), 7.33 (dd, *J* = 7.4, 1.7 Hz, 2H), 7.14 (td, *J* = 7.5, 0.9 Hz, 2H), 7.00 (d, *J* = 7.5 Hz, 2H), 6.97 (d, *J* = 8.4 Hz, 2H), 6.84 (d, *J* = 7.9 Hz, 2H), 5.75 (s, 2H), 4.20 (dt, *J* = 14.1, 7.2 Hz, 2H), 4.07 (dt, *J* = 13.8, 7.0 Hz, 2H), 3.79 – 3.66 (m, 6H), 3.61 (td, *J* = 8.9, 2.9 Hz, 2H), 1.74– 1.64 (dq, *J* = 14.1, 6.9 Hz, 2H), 1.33 – 1.28 (m, 16H), 1.21 – 1.16 (m, 6H), 1.13-1.12 (m, 18H), 1.10 – 1.05 (m, 4H), 0.91 (t, *J* = 7.0 Hz, 6H), 0.74 (m, 2H), 0.51 – 0.25 (m, 8H).

^{13}C NMR (126 MHz, $CDCl_3$) δ 158.5, 157.0, 146.6, 146.6, 141.8, 134.2, 134.1, 133.4, 132.8, 132.2, 131.6 130.5, 130.16, 130.13, 129.8, 129.37, 129.33, 128.9, 127.6, 127.0, 126.9, 122.3, 121.4, 120.17, 120.12, 119.0, 115.5, 115.2, 113.7, 111.7, 83.6, 79.1, 78.7, 78.1, 69.0, 67.8, 49.9, 31.7, 30.8, 29.9, 29.69, 29.66, 29.3, 29.0, 28.9, 28.5, 28.4, 26.3, 25.5, 25.1, 22.6, 14.0.

UV-vis ($CHCl_3$): λ_{max} (ε) = 329(170365), 343 (2262851), 371 (71429), 391 (85867), 424 (50527), 453 (58617), 483 nm (61687 M^{-1} cm^{-1}).

*Synthesis of M,M-**4-C6***

Reaction of *M*-**5-C6** (10 mg, 0.012 mmol), $Pd(PPh_3)_4$ (1.38 mg, 0.0012 mmol) and CuI (0.45 mg, 0.0024 mmol) in Et_3N/THF (1.5ml/2.5mL) furnished *M*,*M*-**4-C6** (9.6 mg, yield = 96%) as a yellow solid with green emission under a 365 nm lamp.

*Synthesis of P,P-**4-C4***

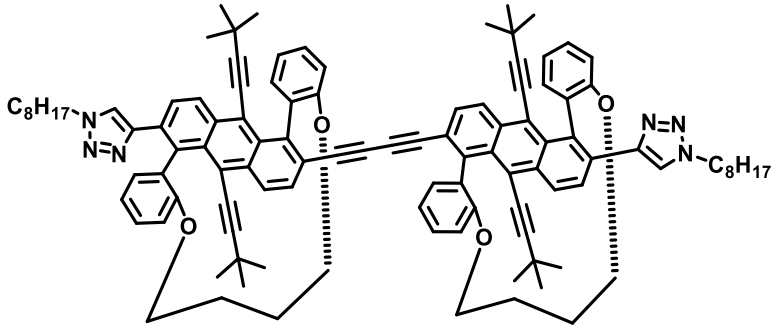

Reaction of *P*-**5-C4** (10mg, 0.013 mmol), $Pd(PPh_3)_4$ (1.50 mg, 0.0013 mmol) and CuI (0.49 mg, 0.0026 mmol) in Et_3N/THF (1ml/3mL) furnished *P*,*P*-**4-C4** (9.6 mg, yield = 96%) as a yellow solid with green emission under a 365 nm lamp.

^{1}H NMR (500 MHz, $CDCl_3$) δ 8.46 (d, *J* = 9.2 Hz, 2H), 8.31 (d, *J* = 9.0 Hz, 2H), 8.24 (d, *J* = 9.2 Hz, 2H), 7.92 (dd, *J* = 7.5, 1.7 Hz, 2H), 7.50 (m, 2H), 7.46 (m, 2H), 7.41 (tdd, *J* = 9.5, 8.0, 1.7 Hz, 4H), 7.13 (td, *J* = 7.5, 0.8 Hz, 2H), 6.96 (td, *J* = 7.5, 0.8 Hz, 2H), 6.78 (d, *J* = 8.0 Hz, 2H), 6.69 (d, *J* = 7.9 Hz, 1H), 5.94 (s, 2H), 4.23 (dt, *J* = 14.1, 7.2 Hz, 2H), 4.08 (dt, *J* = 13.8, 7.0 Hz, 2H), 3.67 (m, 4H), 3.41 ((m, 2H), 3.32 (m, 2H), 1.76 (m, 4H), 1.33 – 1.25 (m, 20H), 1.12 – 1.11 (br, 36H), 0.91 (t, *J* = 7.0 Hz, 6H), 0.77 (m, 4H), 0.61 – 0.51 (m, 4H).

^{13}C NMR (126 MHz, $CDCl_3$) δ 156.9, 155.7, 146.3, 140.9, 133.3, 133.1, 133.0, 132.4, 132.3, 131.7, 131.5, 129.7, 129.2, 129.1, 129.0, 128.9, 127.3, 126.4, 125.9 122.4, 120.3, 120.2, 119.81, 118.8, 118.0, 114.2, 113.9, 111.3, 110.0, 83.5, 78.9, 66.6, 65.9, 49.9, 31.7, 30.78, 30.76, 30.0, 29.0, 28.9, 28.4, 28.3, 26.3, 26.1, 25.9, 22.6, 14.0.

MS (MALDI-TOF, m/z): calcd for $C_{108}H_{112}N_6O_4$, 1557.877; found 1557.952.

UV-vis ($CHCl_3$): λ_{max} (ε) = 332 (136288), 346 (206869), 373 (63628), 394 (70941), 428 (40195), 457 (47180), 488 nm (47788 M^{-1} cm^{-1}).

S3 Characterization of 4-Cn

This section presents the ^{1}H NMR, ^{13}C NMR, COSY NMR, HSQC NMR, and HMBC NMR spectra of the **4-Cn** series.

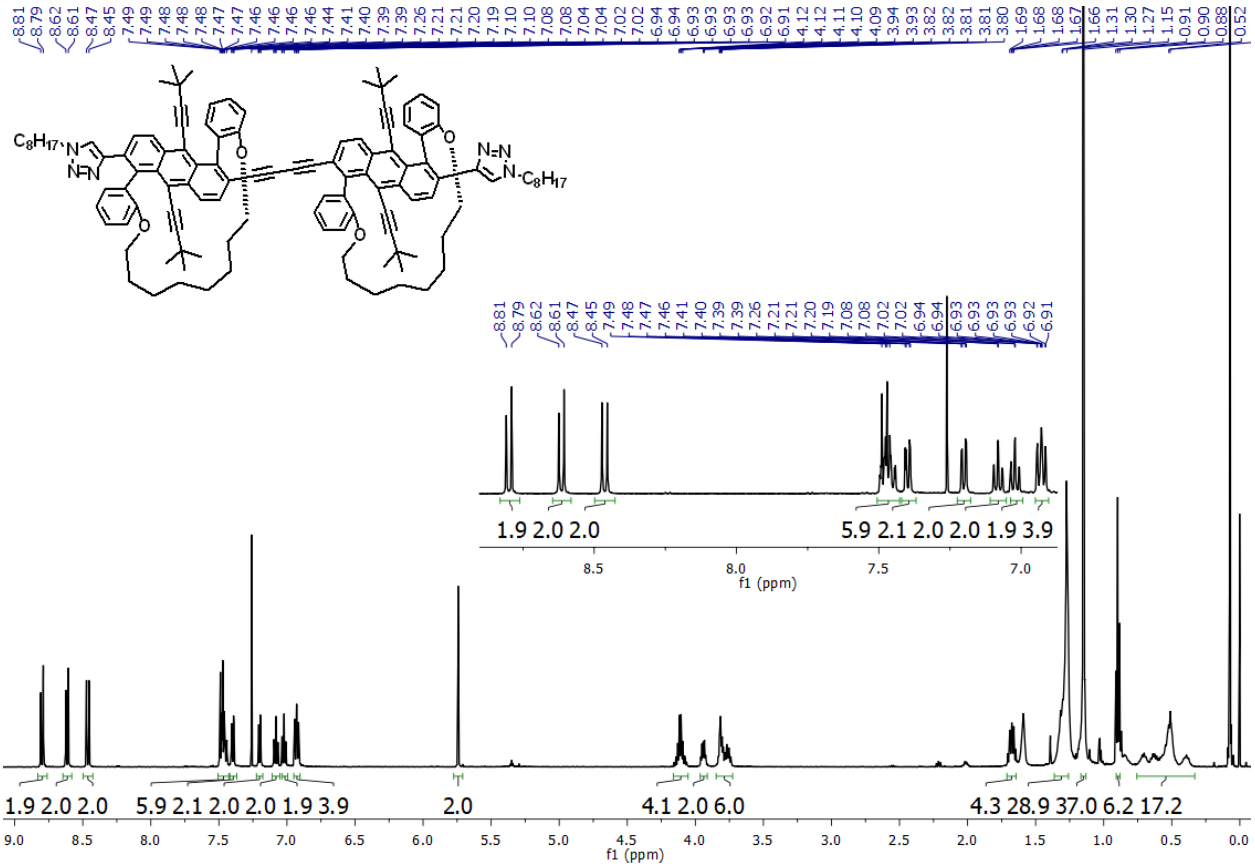

Figure S1. ^{1}H NMR (500 MHz) of *P*,*P*-**4-C8** in $CDCl_3$, measured at 298 K.

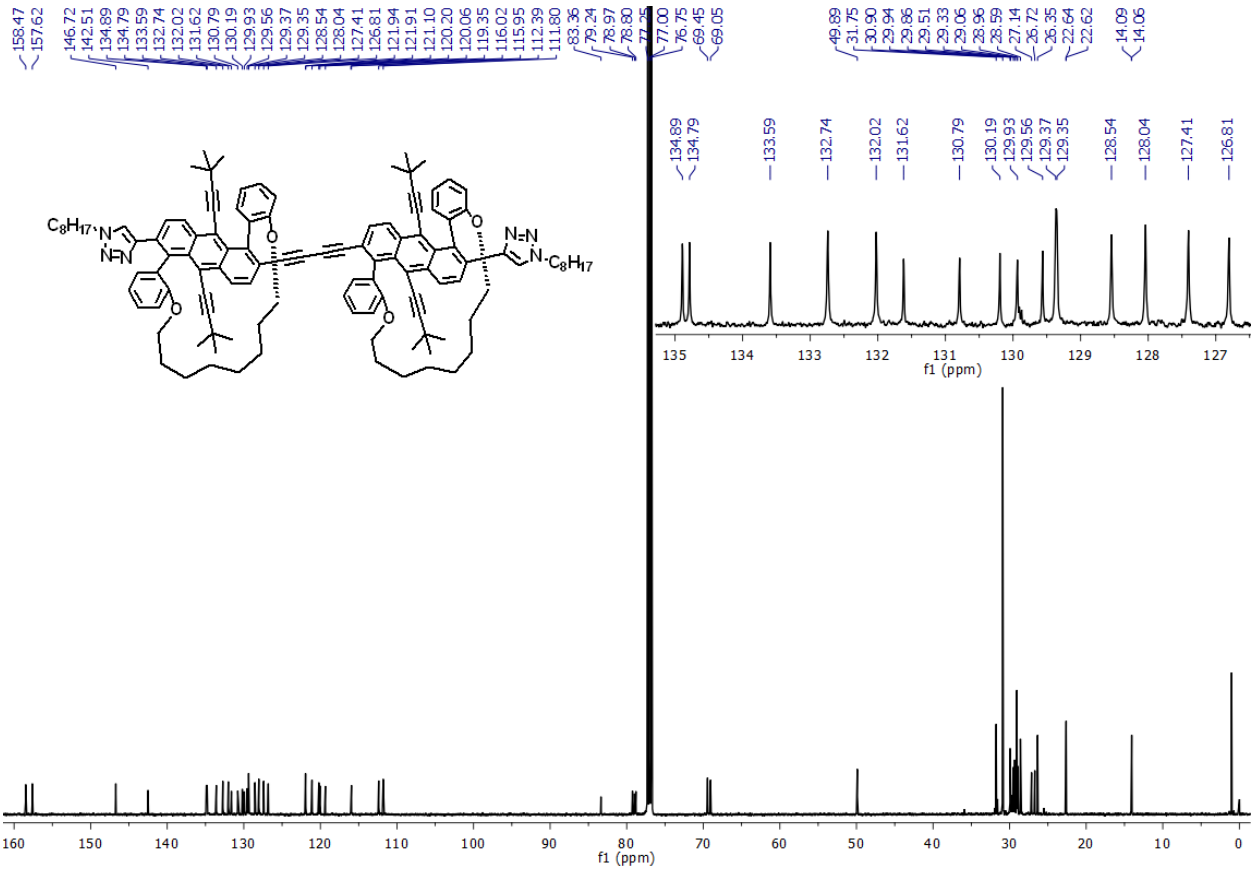

Figure S2. ^{13}C NMR (126 MHz) of *P,P*-**4-C8** in $CDCl_3$, measured at 298 K.

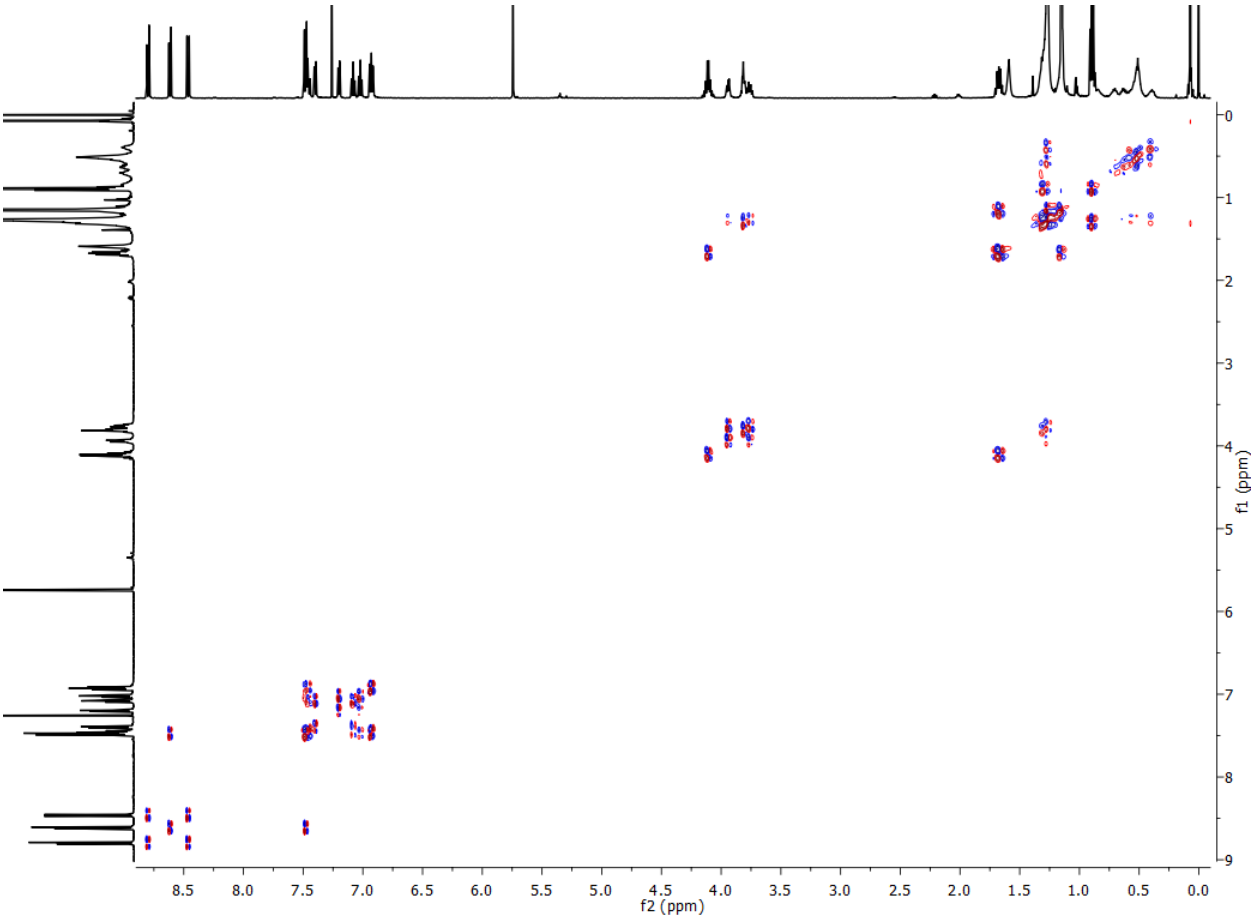

Figure S3. COSY NMR (500 MHz) of *P,P*-**4-C8** in $CDCl_3$, measured at 298 K.

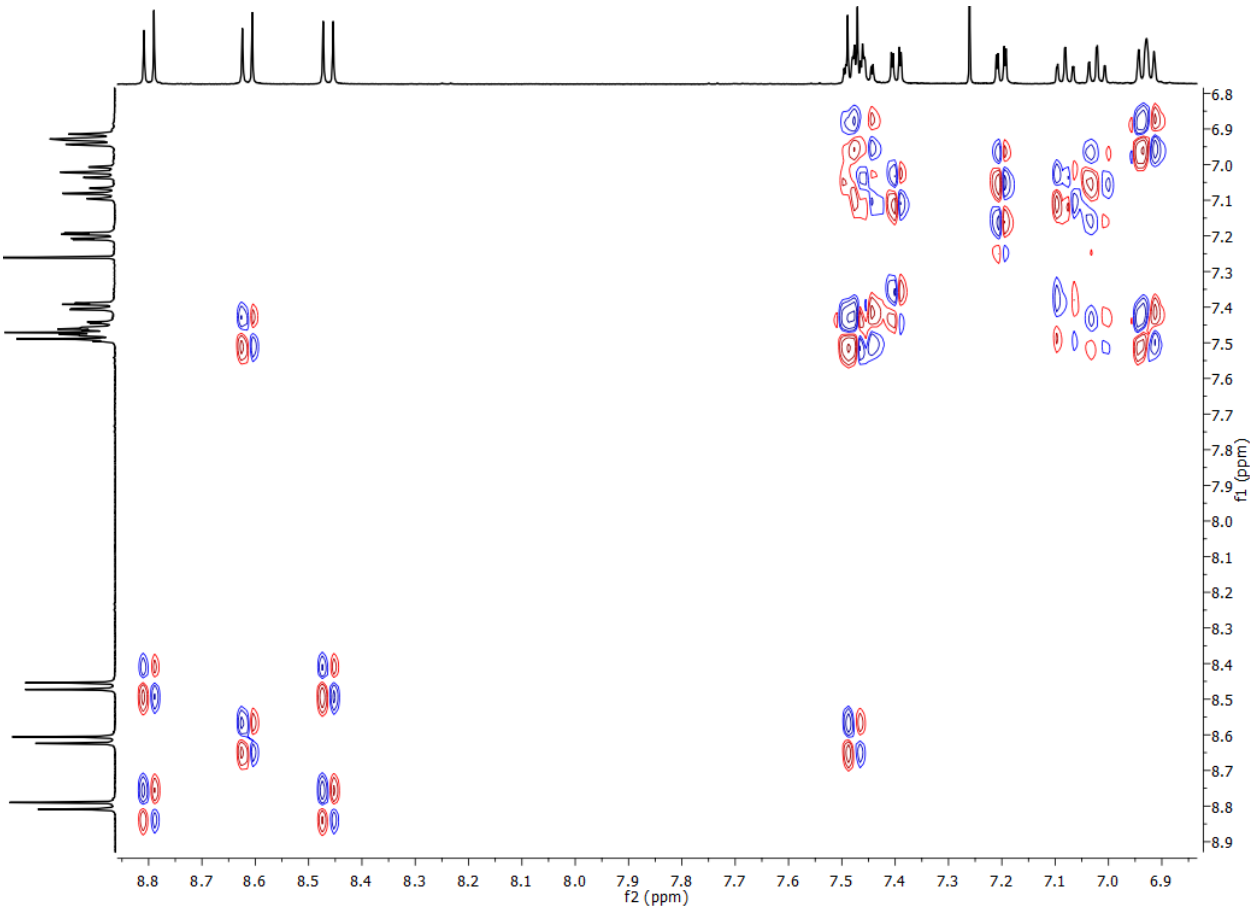

Figure S4. COSY NMR (500 MHz) *P*,*P*-**4-C8** in $CDCl_3$, measured at 298 K (expansion in aromatic region).

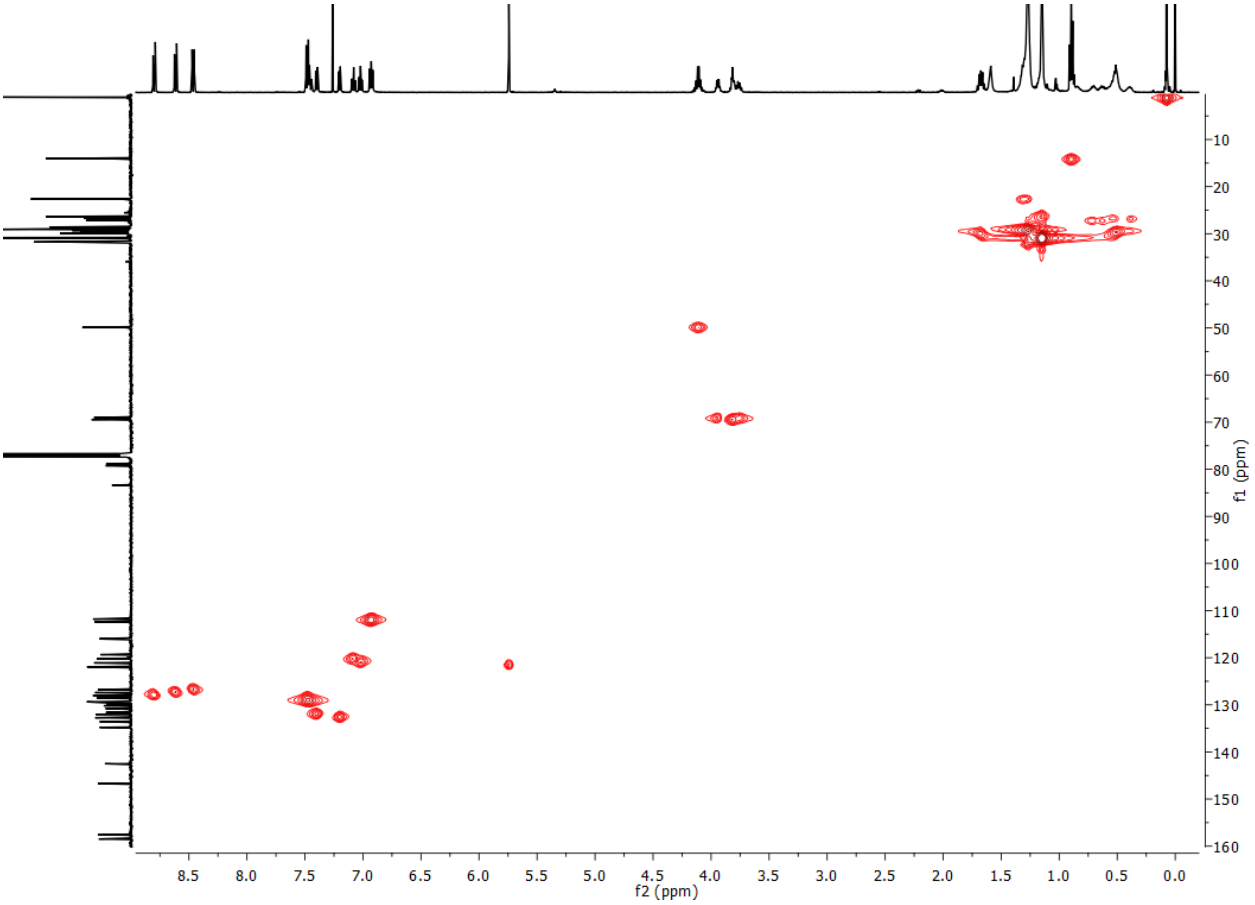

Figure S5. HSQC NMR (500 MHz) of *P*,*P*-**4-C8** in $CDCl_3$, measured at 298 K.

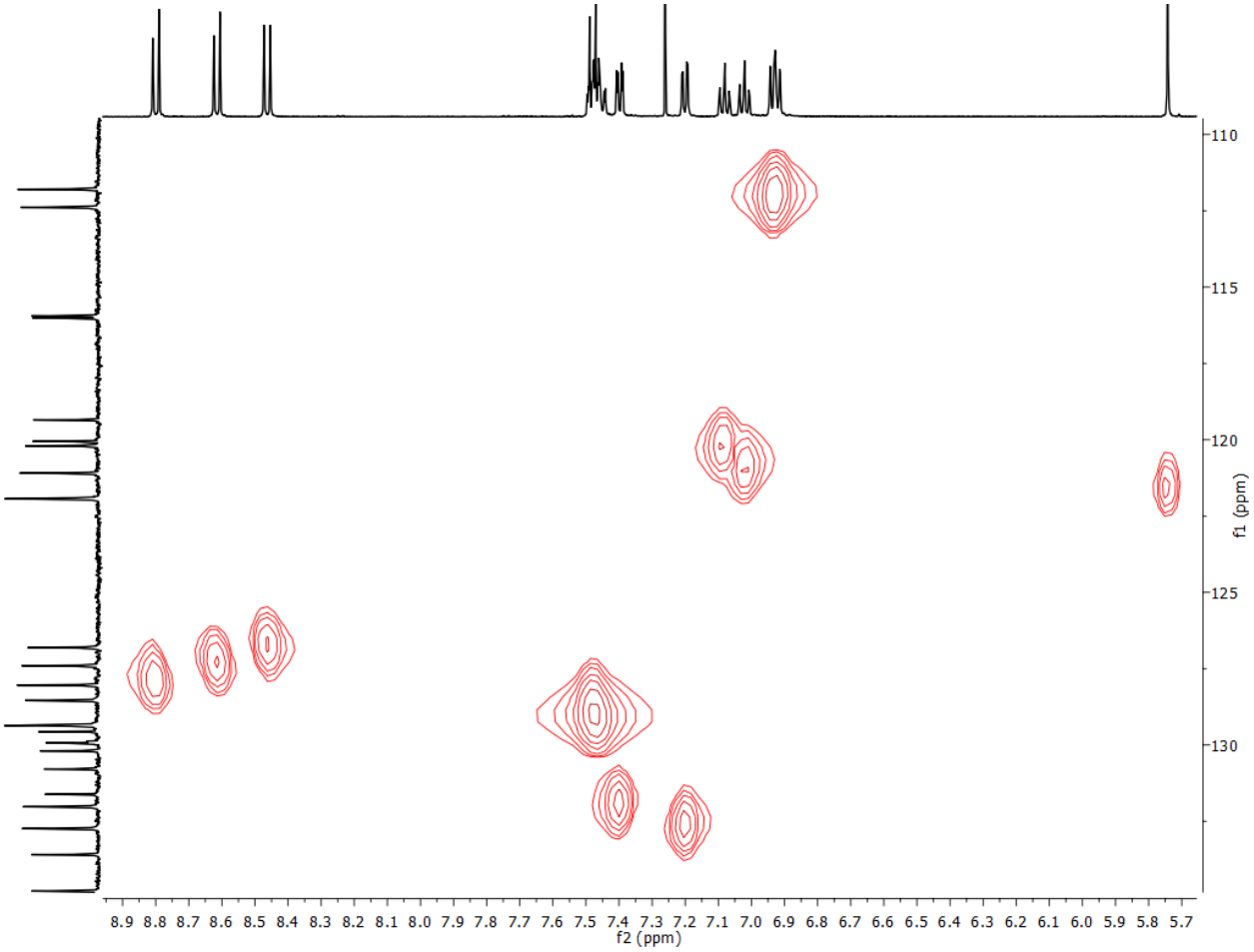

Figure S6. HSQC NMR (500 MHz) *P,P*-**4-C8** in $CDCl_3$, measured at 298 K (expansion in aromatic region).

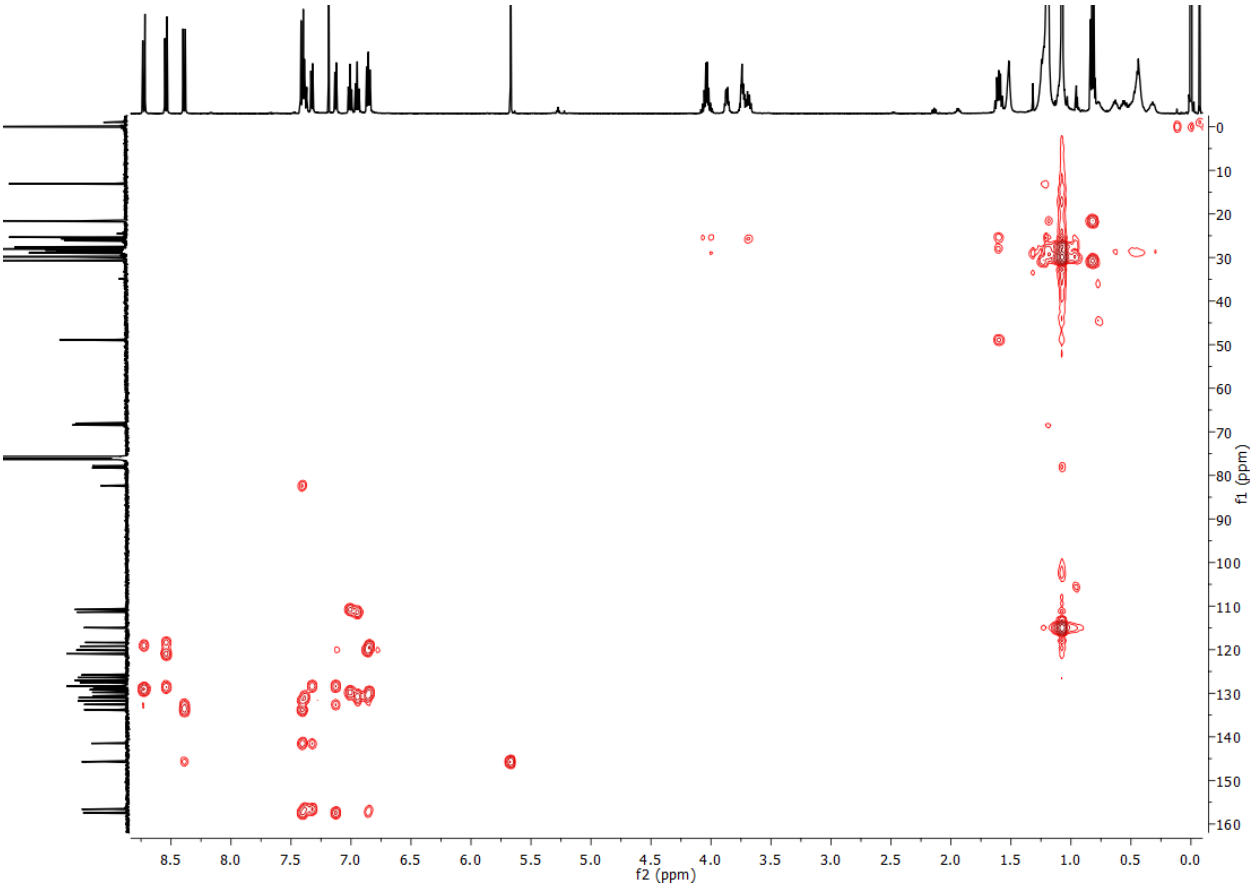

Figure S7. HMBC NMR (500 MHz) of *P,P*-**4-C8** in $CDCl_3$, measured at 298 K.

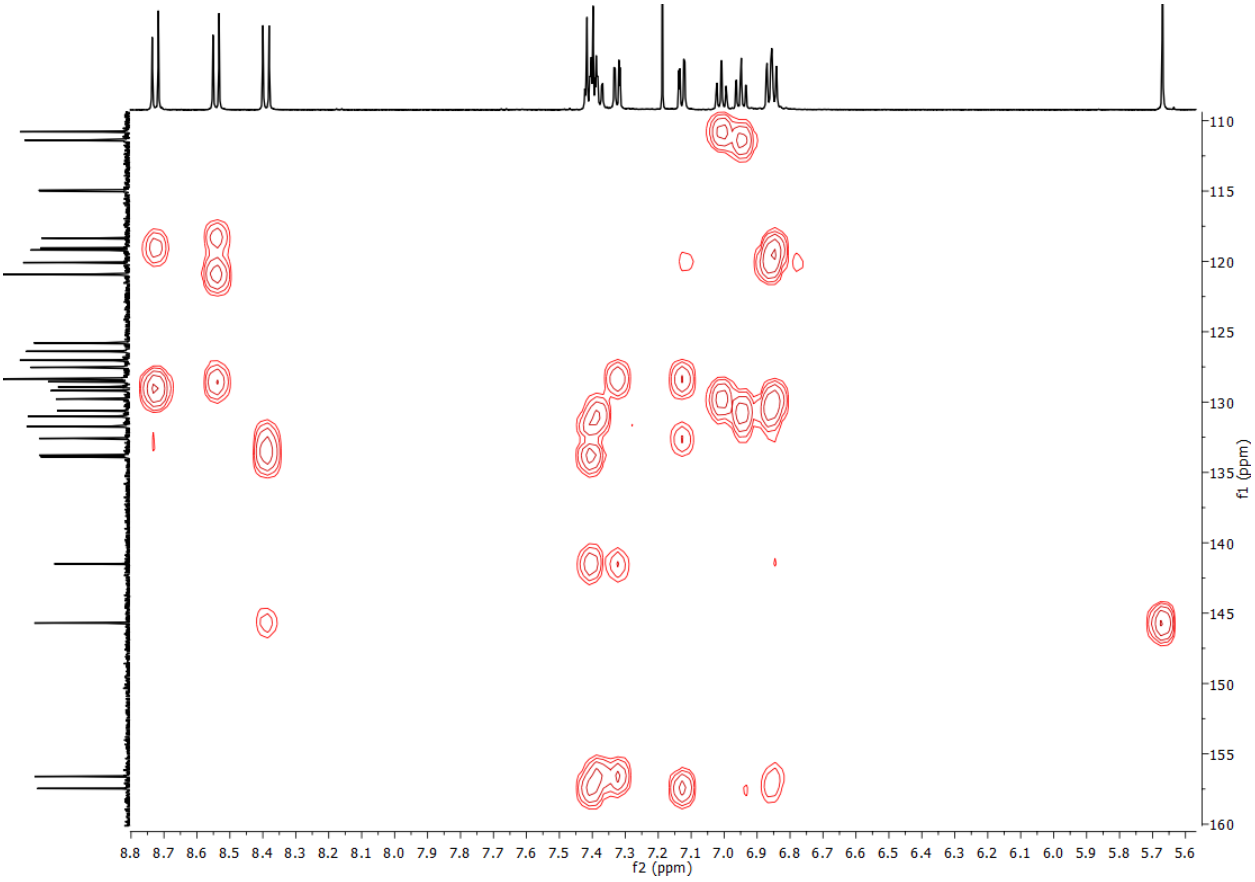

Figure S8. HMBC NMR (500 MHz) of *P*,*P*-**4-C8** in $CDCl_3$, measured at 298 K (expansion in aromatic region).

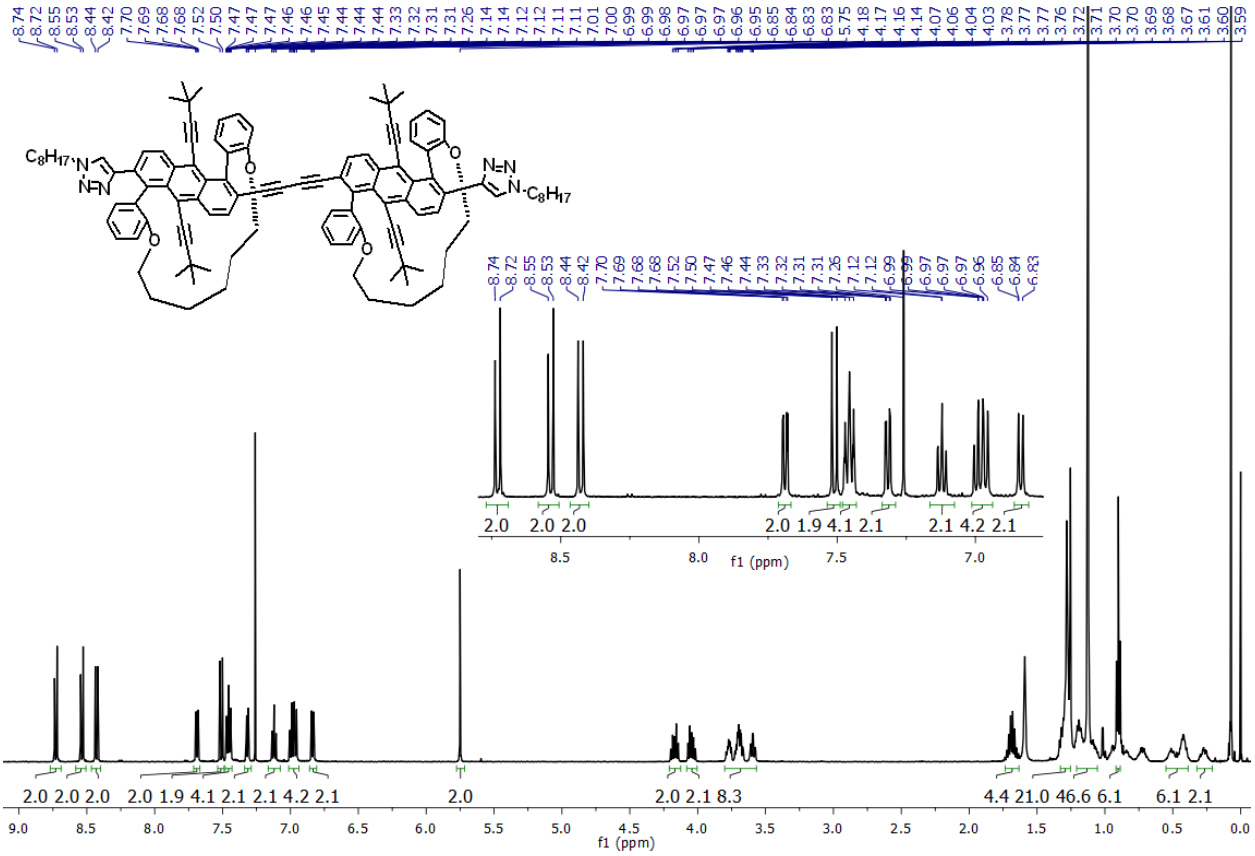

Figure S9. ^{1}H NMR (500 MHz) of *P*,*P*-**4-C6** in $CDCl_3$, measured at 298 K.

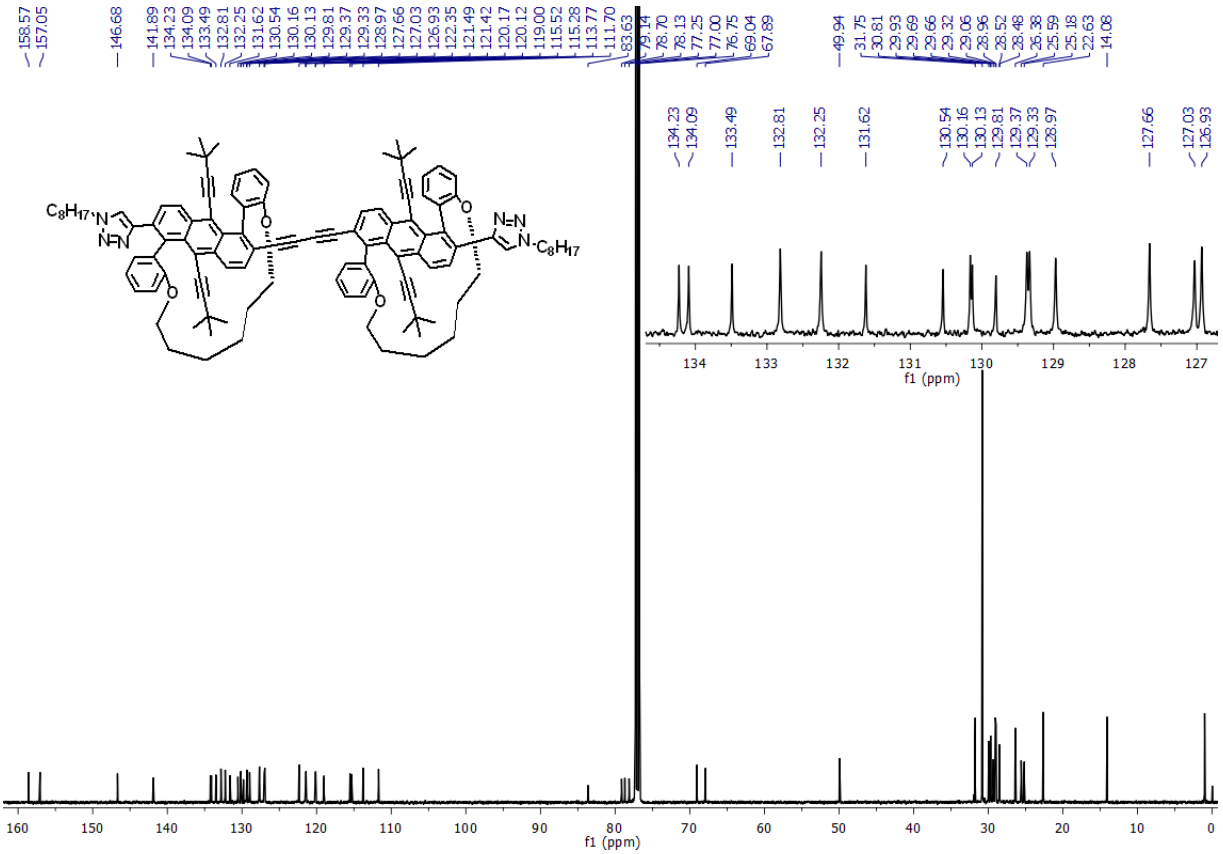

Figure S10. ^{13}C NMR (126 MHz) of *P,P*-**4-C6** in $CDCl_3$, measured at 298 K.

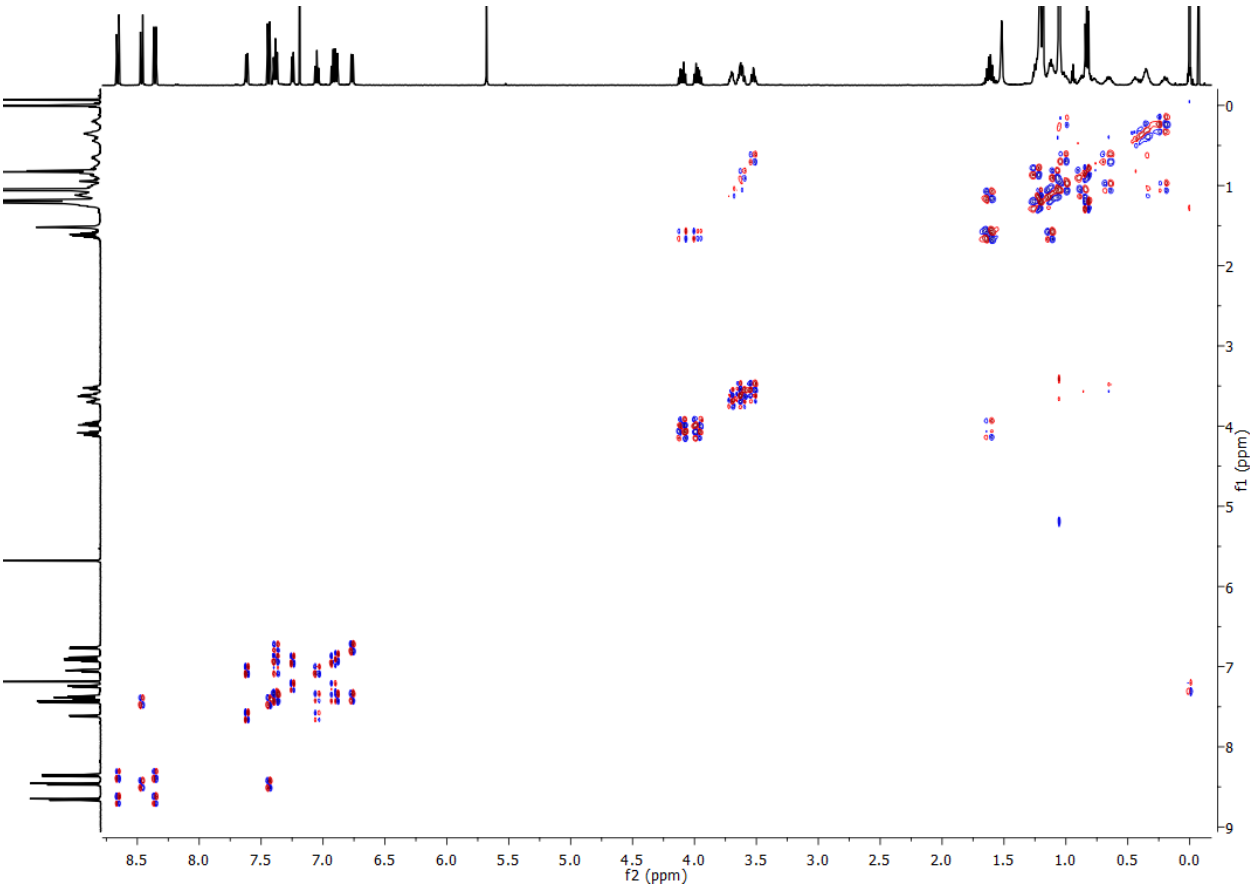

Figure S11. COSY NMR (500 MHz) of *P*,*P*-**4-C6** in $CDCl_3$, measured at 298 K.

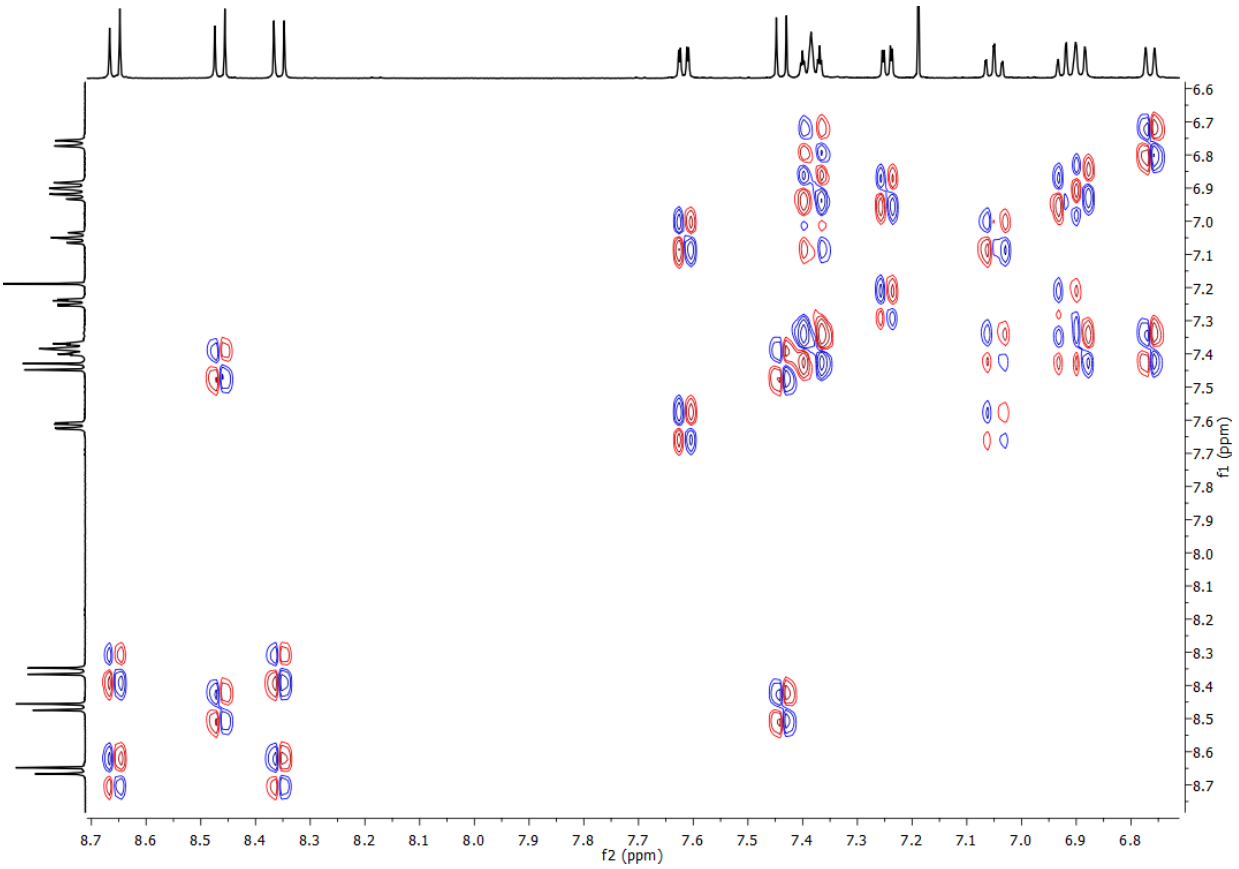

Figure S12. COSY NMR (500 MHz) of *P,P*-**4-C6** in $CDCl_3$, measured at 298 K (expansion in aromatic region).

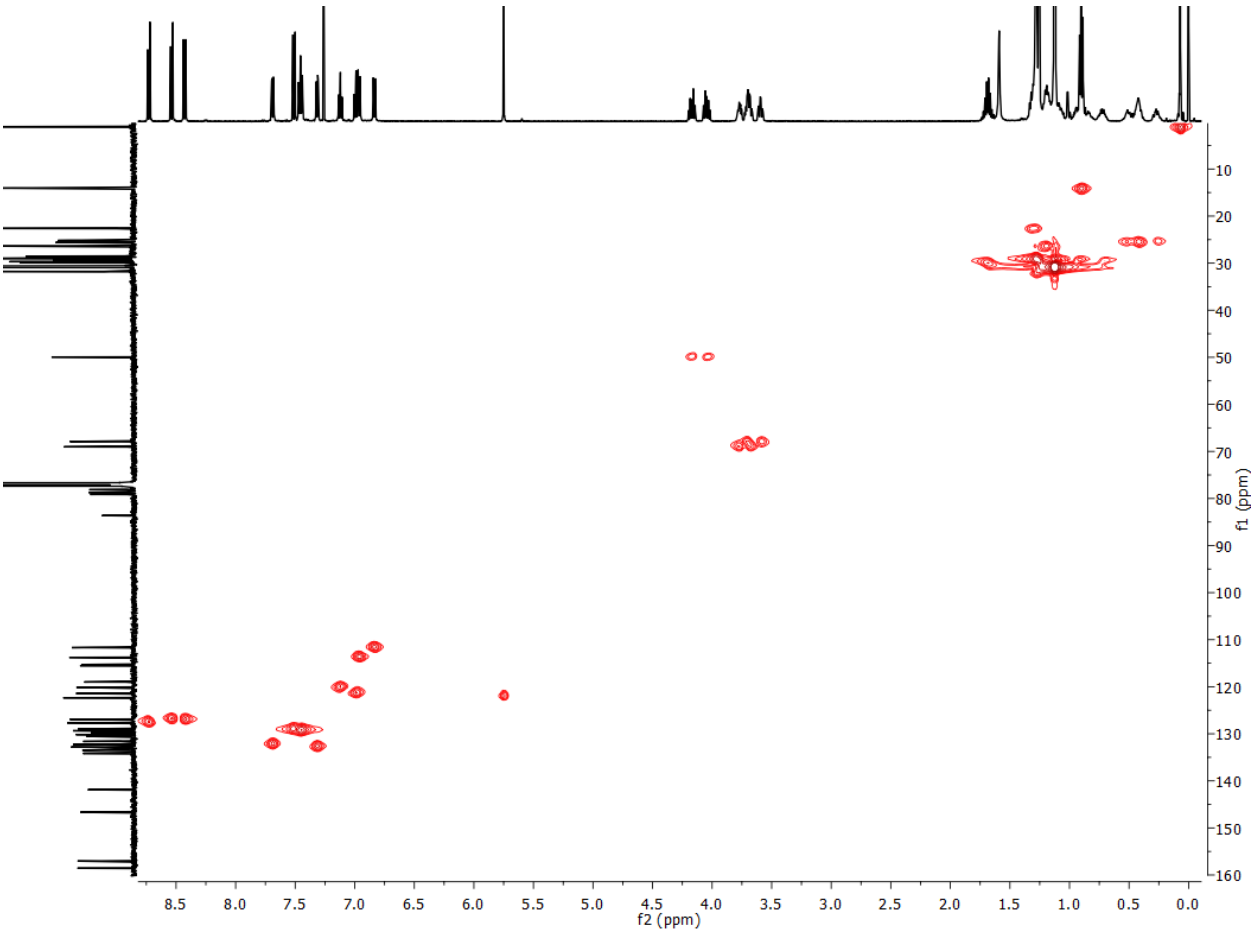

Figure S13. HSQC NMR (500 MHz) of *P*,*P*-**4-C6** in $CDCl_3$, measured at 298 K.

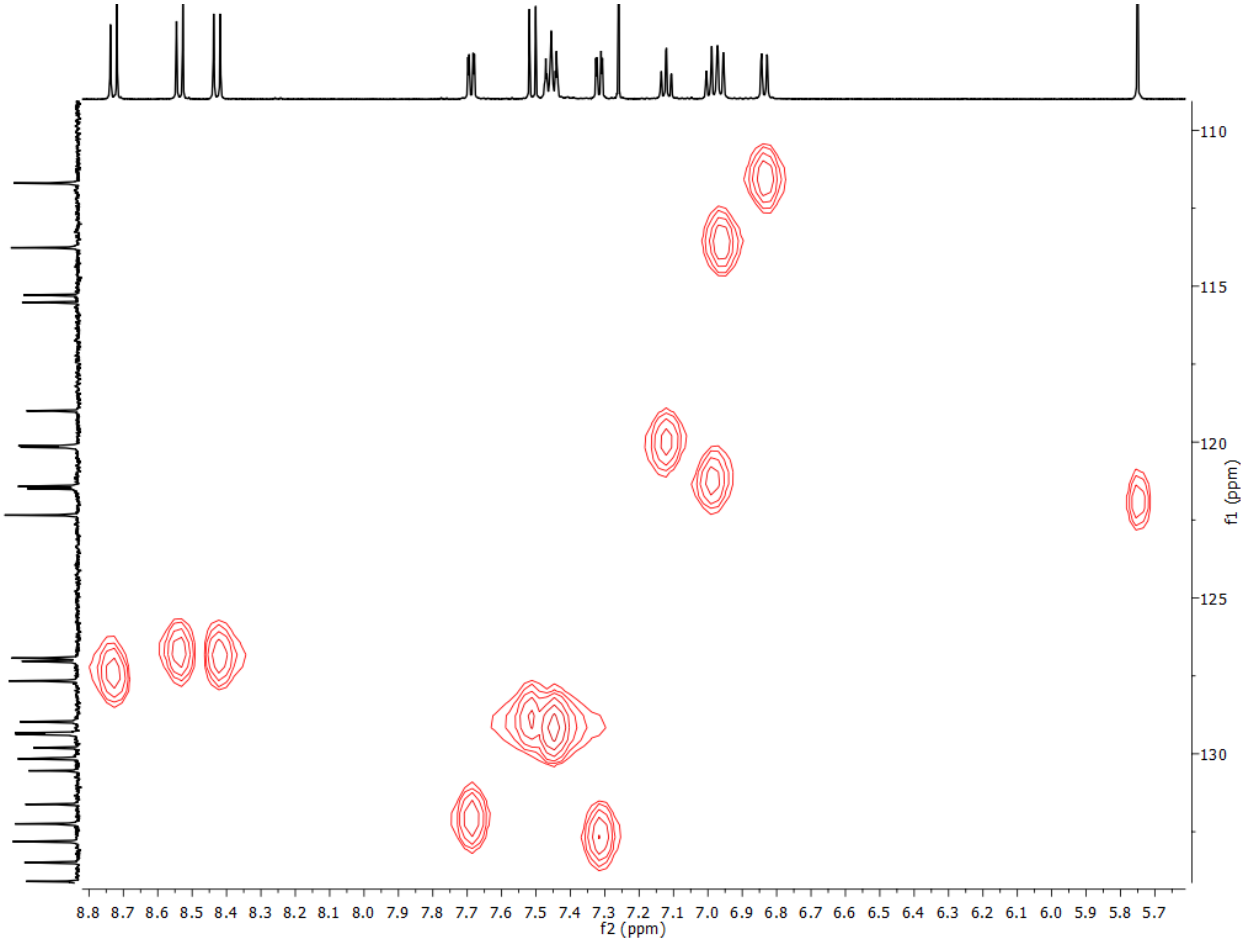

Figure S14. HSQC NMR (500 MHz) of *P*,*P*-**4-C6** in $CDCl_3$, measured at 298 K (expansion in aromatic region).

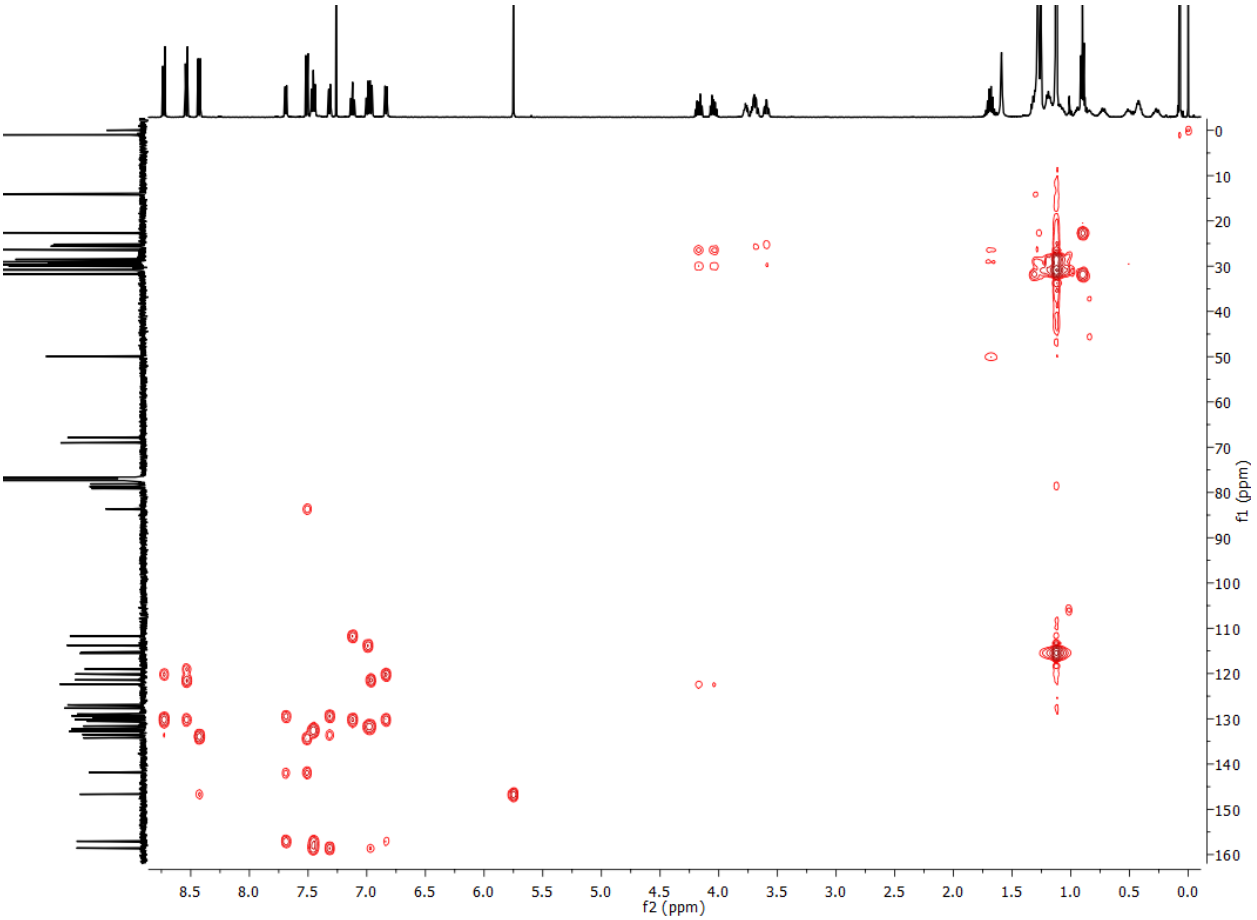

Figure S15. HMBC NMR (500 MHz) of *P*,*P*-**4-C6** in $CDCl_3$, measured at 298 K.

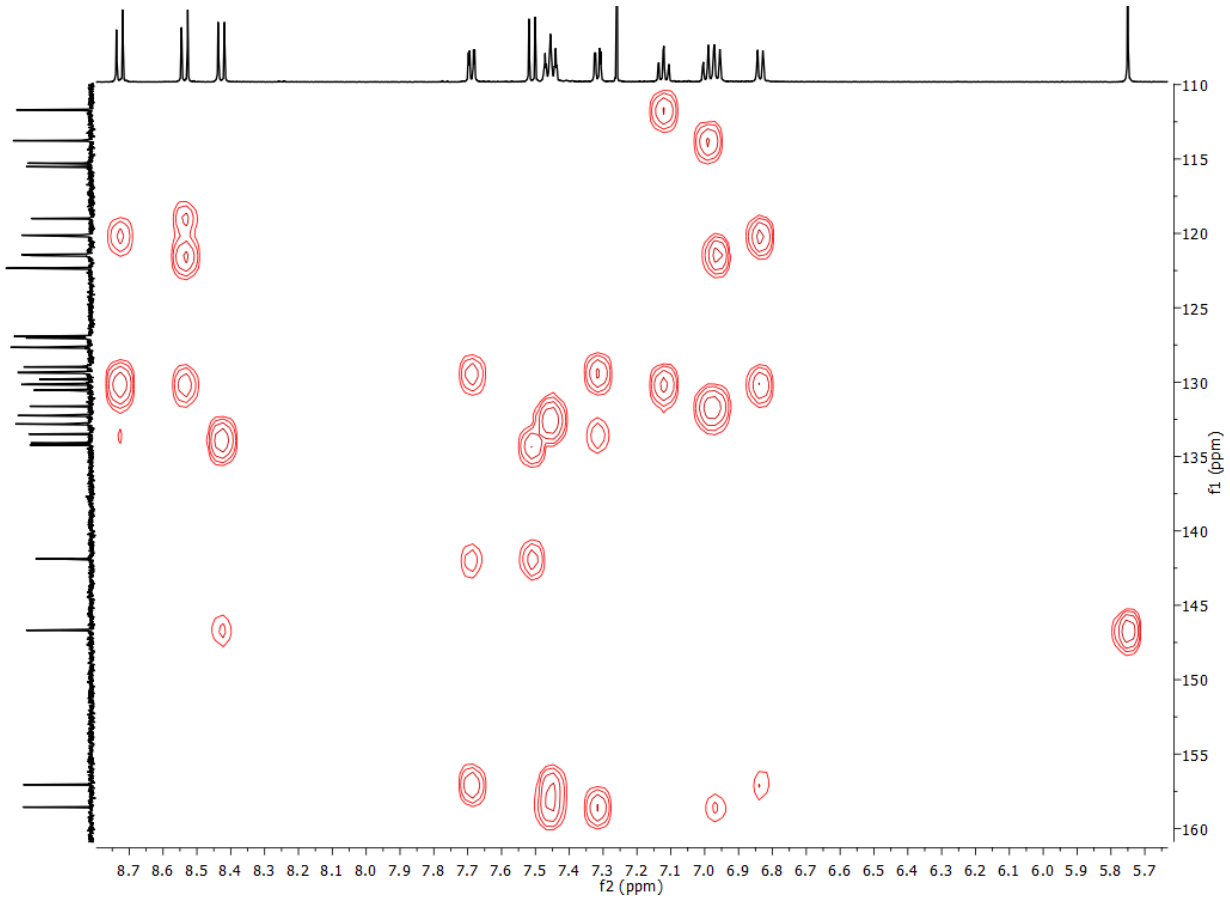

Figure S16. HMBC NMR (500 MHz) of *P*,*P*-**4-C6** in $CDCl_3$, measured at 298 K (expansion in aromatic region).

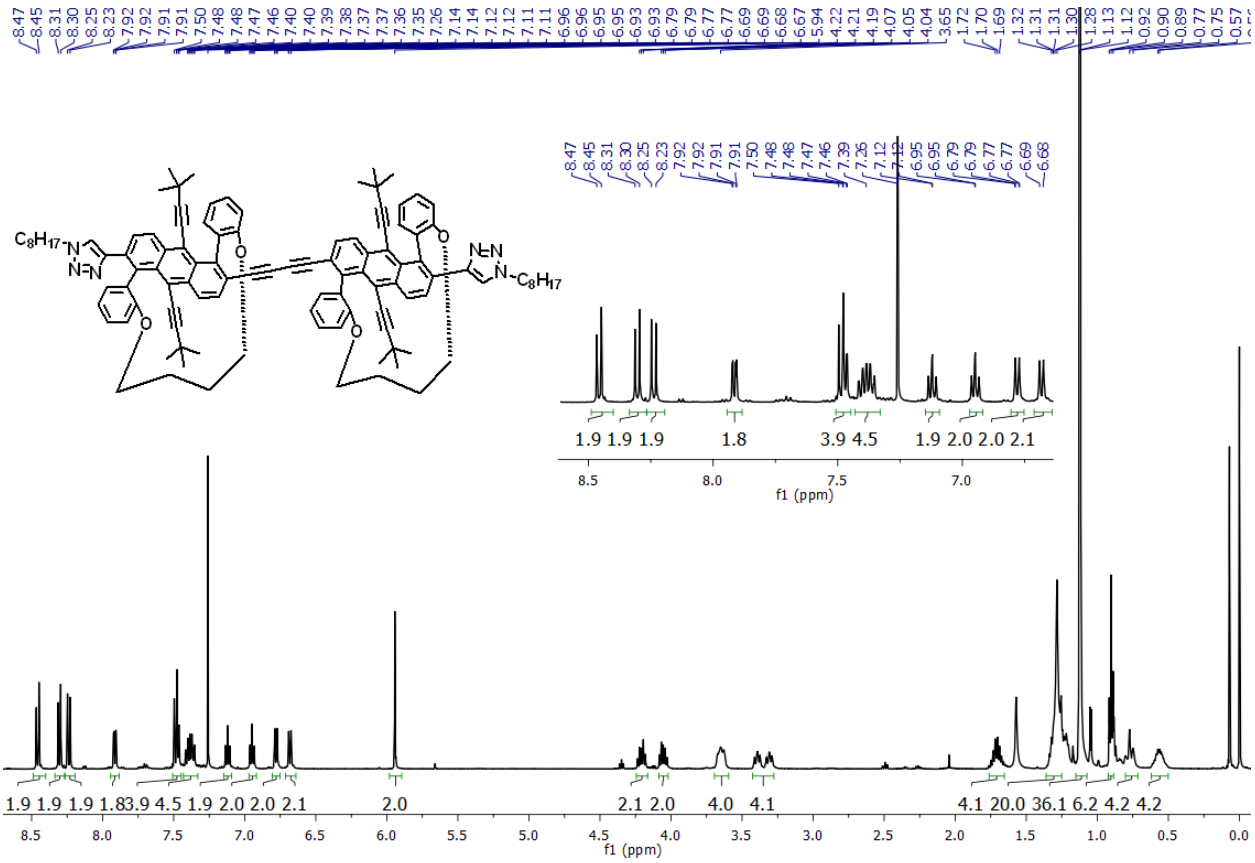

Figure S17. ^{1}H NMR (500 MHz) of *P*,*P*-**4-C4** in $CDCl_3$, measured at 298 K.

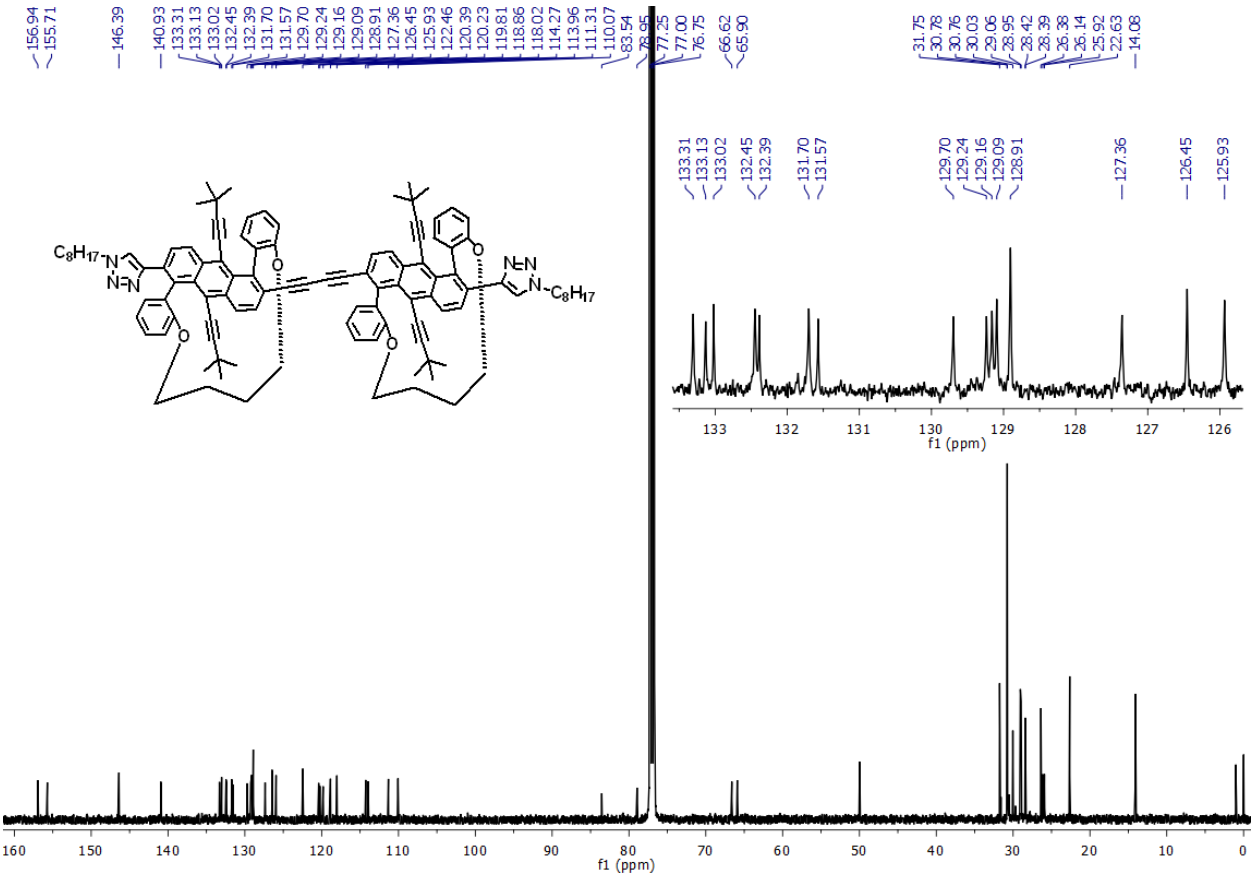

Figure S18. ^{13}C NMR (126 MHz) of *P*,*P*-**4-C4** in $CDCl_3$, measured at 298 K.

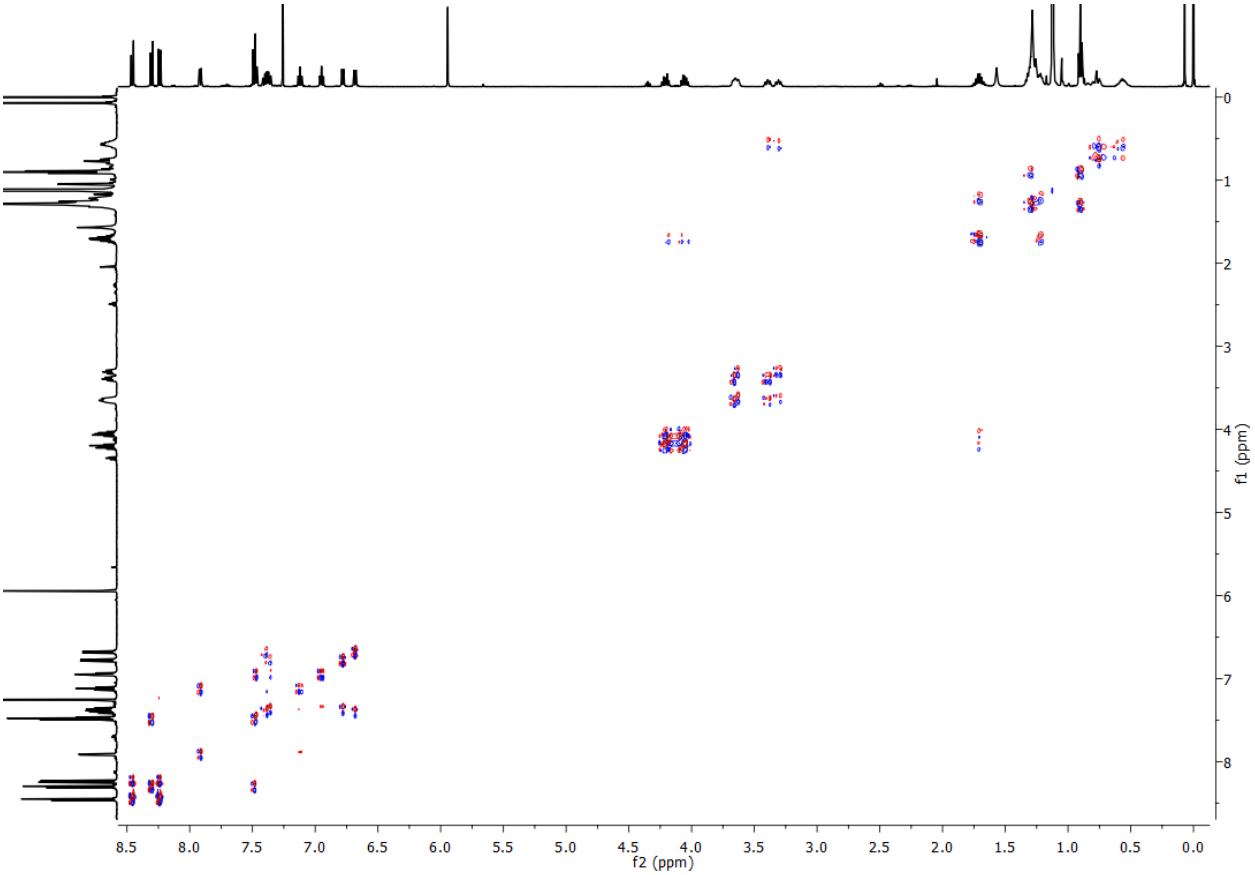

Figure S19. COSY NMR (500 MHz) of *P*,*P*-**4-C4** in $CDCl_3$, measured at 298 K.

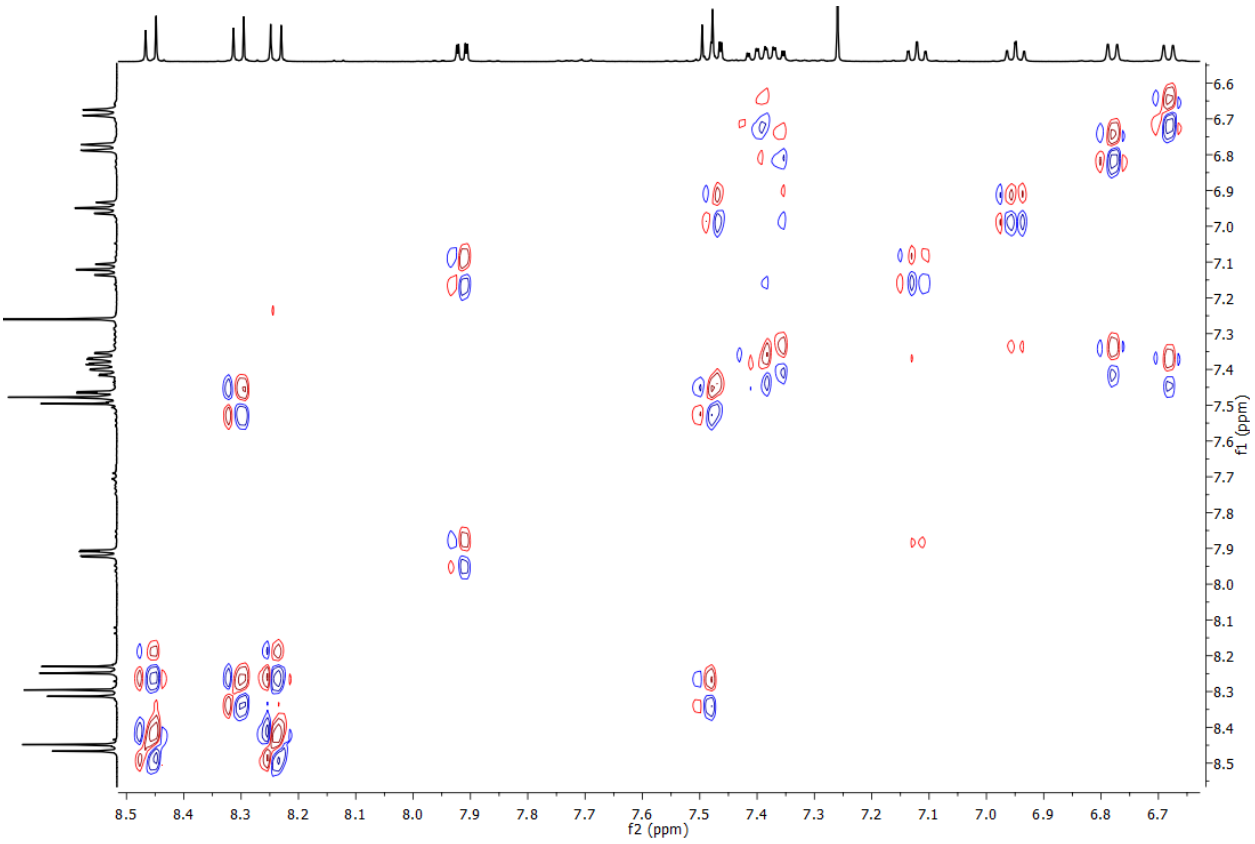

Figure S20. COSY NMR (500 MHz) of *P,P*-**4-C4** in $CDCl_3$, measured at 298 K (expansion in aromatic region).

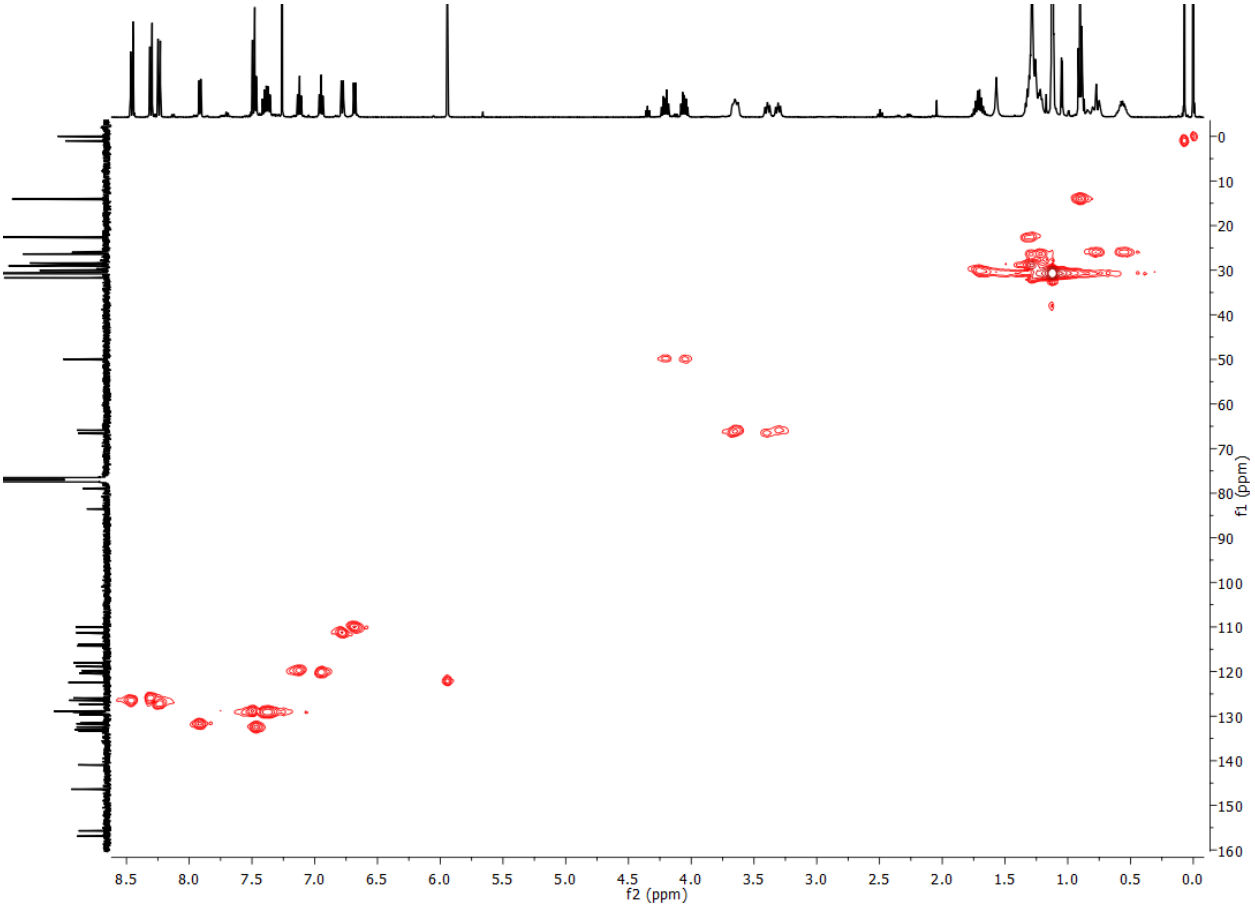

Figure S21. HSQC NMR (500 MHz) of *P*,*P*-**4-C4** in $CDCl_3$, measured at 298 K.

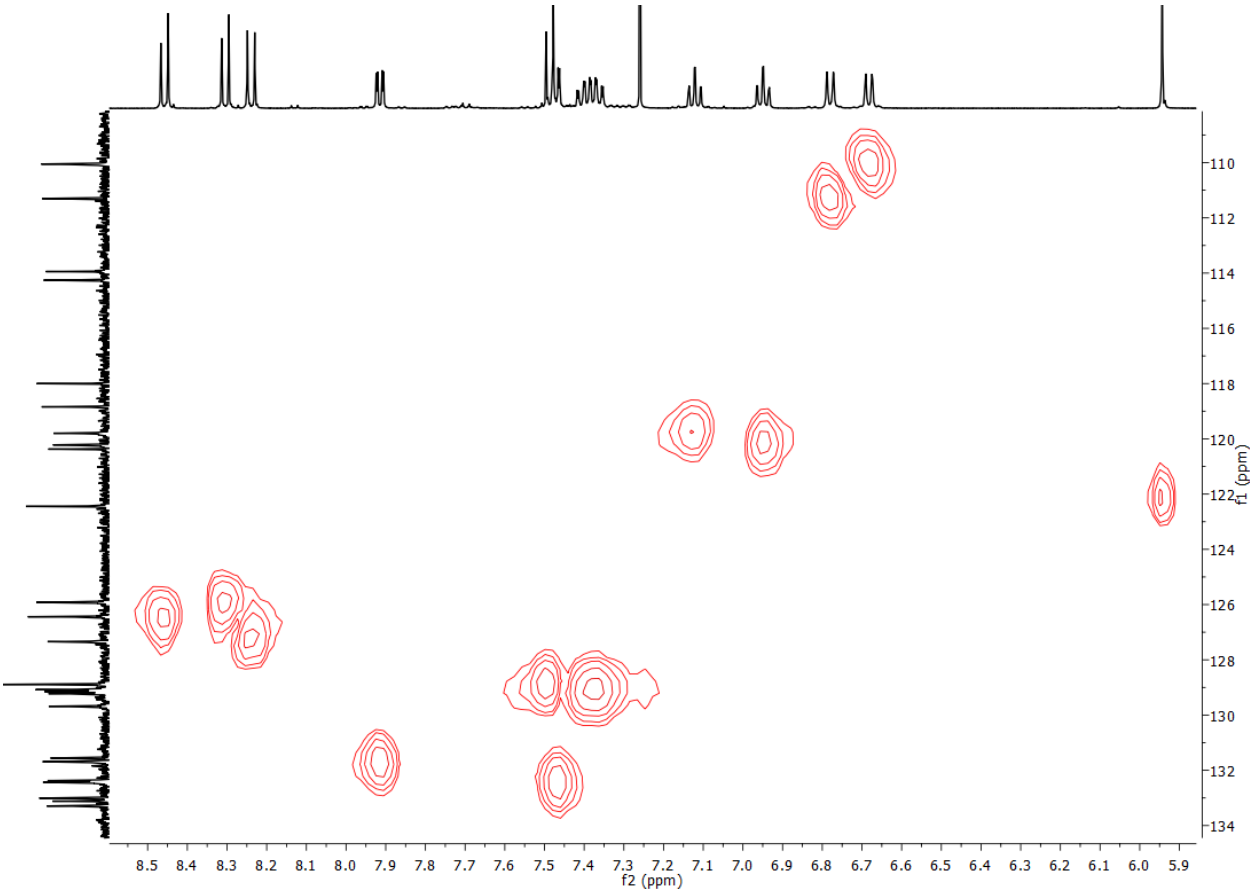

Figure S22. HSQC NMR (500 MHz) of *P*,*P*-**4-C4** in $CDCl_3$, measured at 298 K (expansion in aromatic region).

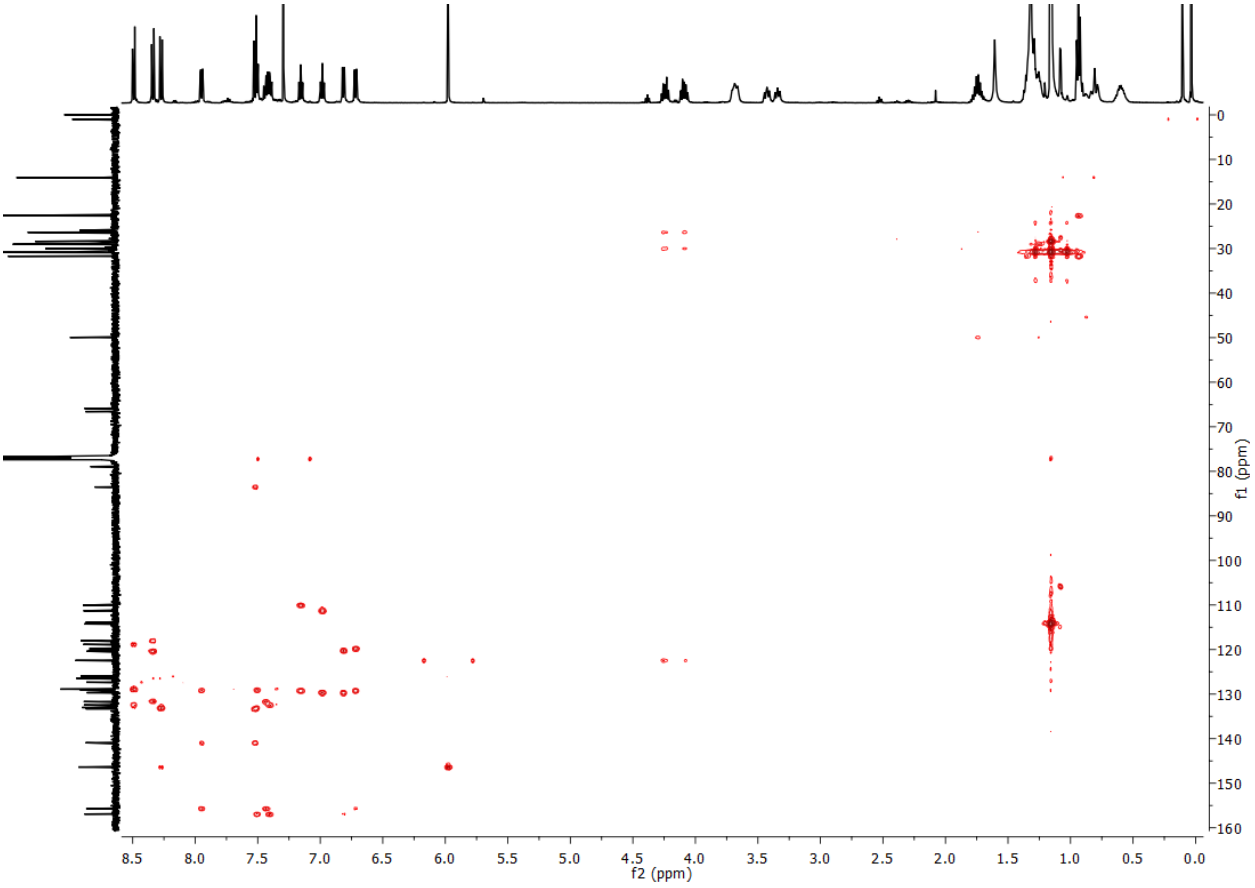

Figure S23. HMBC NMR (500 MHz) of *P*,*P*-**4-C4** in $CDCl_3$, measured at 298 K.

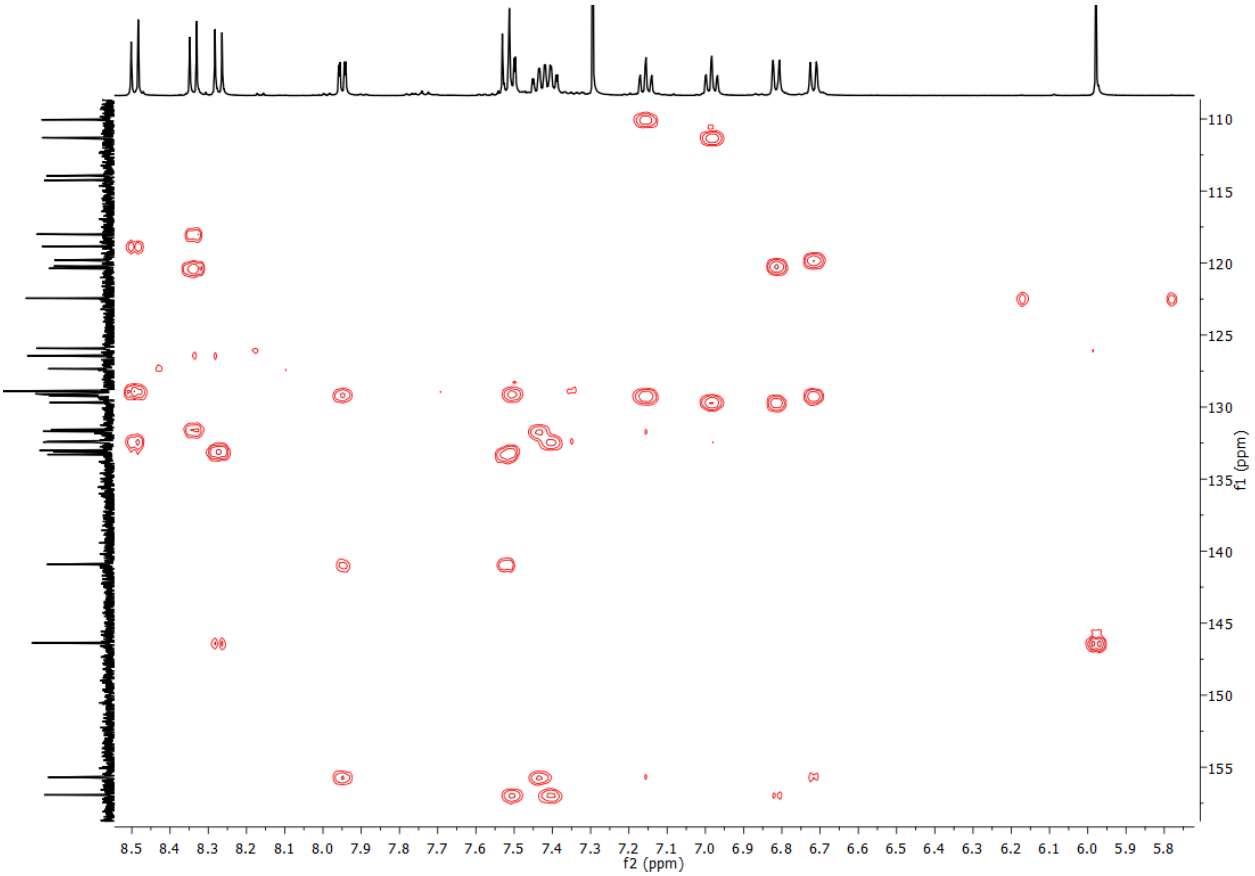

Figure S24. HMBC NMR (500 MHz) of *P*,*P*-**4-C4** in $CDCl_3$, measured at 298 K (expansion in aromatic region).

S4 Photophysical properties

All photophysical studies were performed with dilute solutions of the compounds while keeping the absorbance from the lowest energy band at ~0.05 to exclude self-absorption.

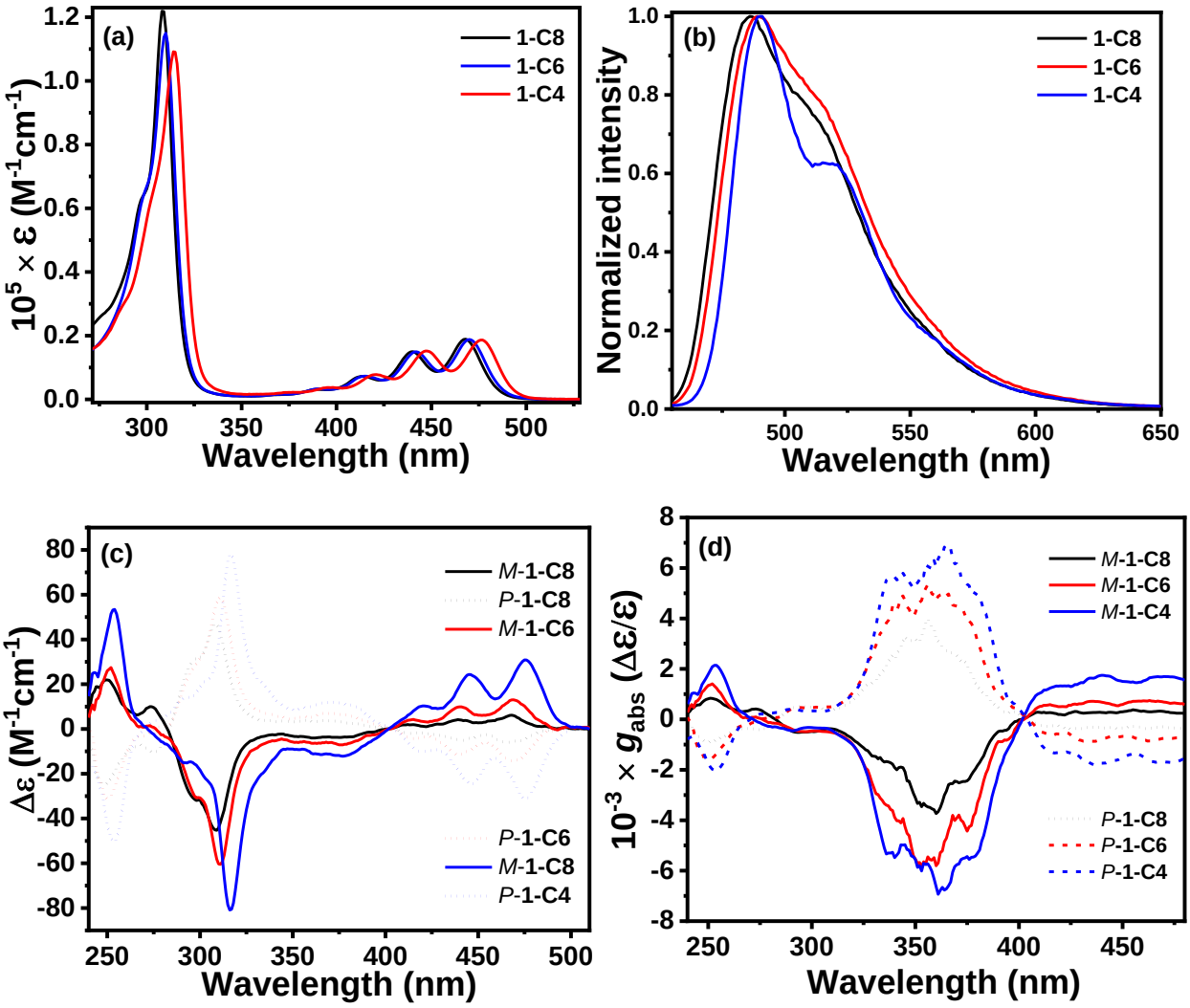

Figure S25. Photophysical and chiroptical properties of **1-Cn** in chloroform at room temperature. (a) quantitative UV-vis spectra, (b) normalized emission spectra, (c) circular dichroism spectra and (d) g_{abs} values.

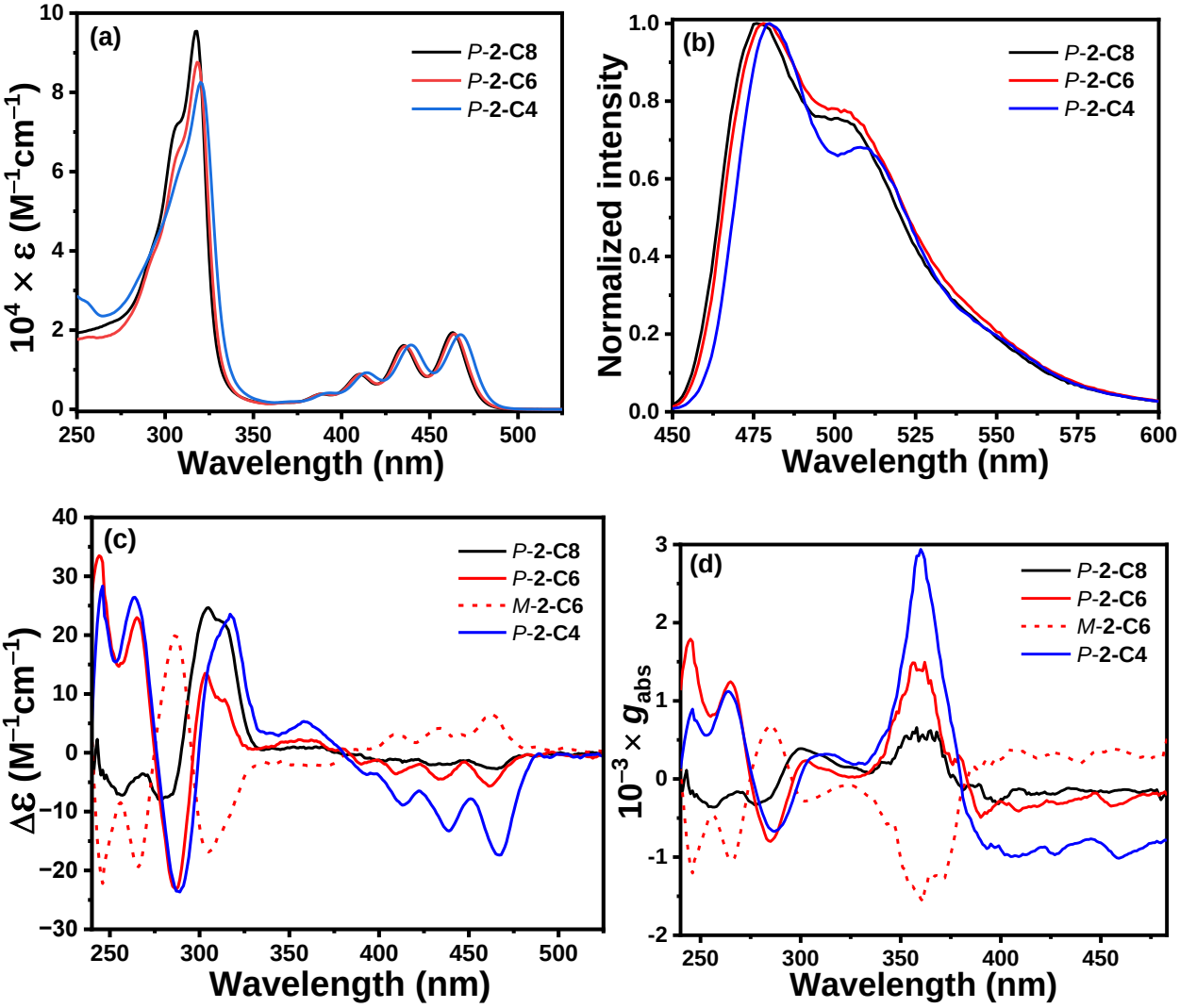

Figure S26. Photophysical and chiroptical properties of **2-Cn** in chloroform at room temperature. (a) quantitative UV-vis spectra, (b) normalized emission spectra, (c) circular dichroism spectra and (d) g_{abs} values.

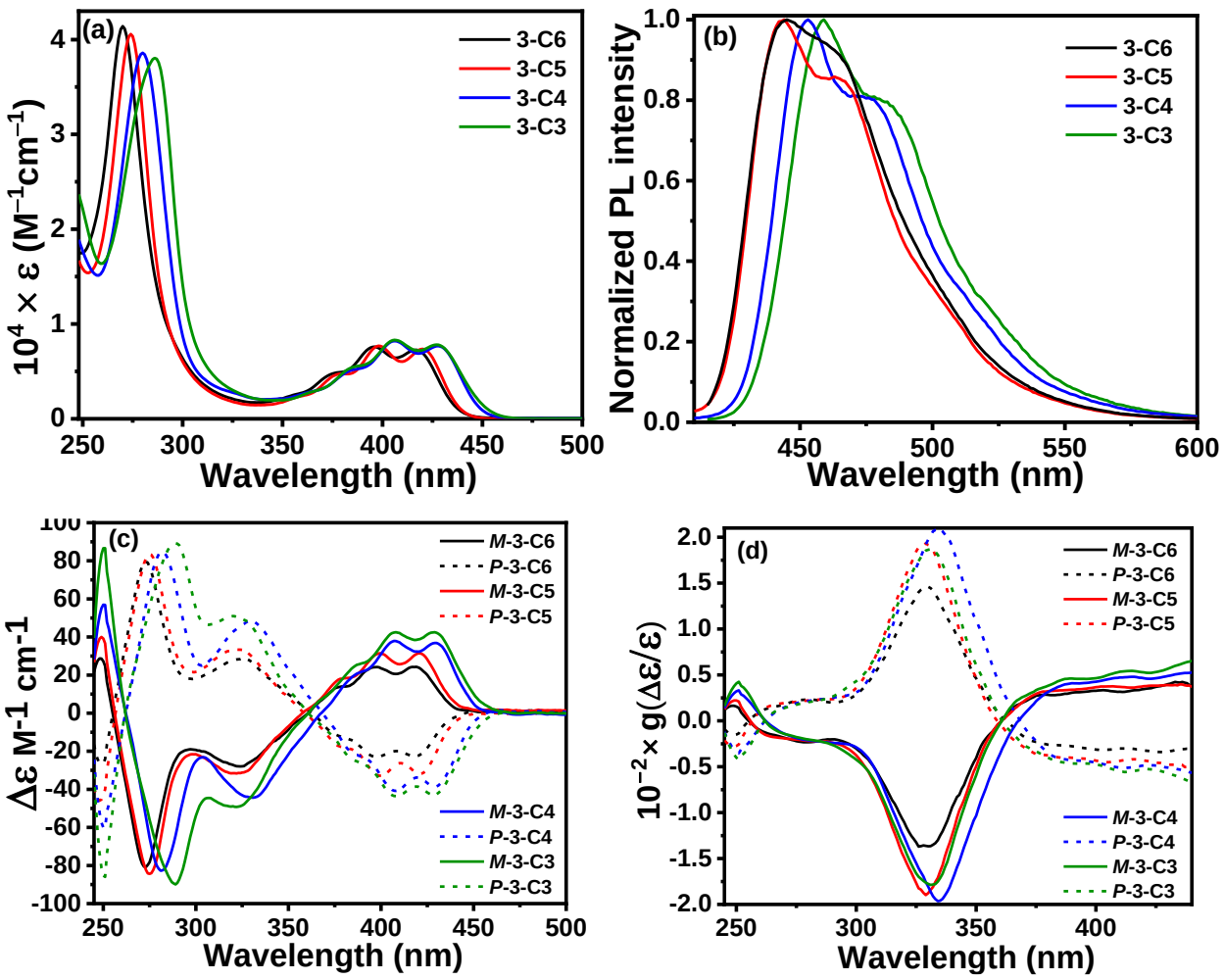

Figure S27. Photophysical and chiroptical properties of **3-Cn** in chloroform at room temperature. (a) quantitative UV-vis spectra, (b) normalized emission spectra, (c) circular dichroism spectra and (d) g_{abs} values.

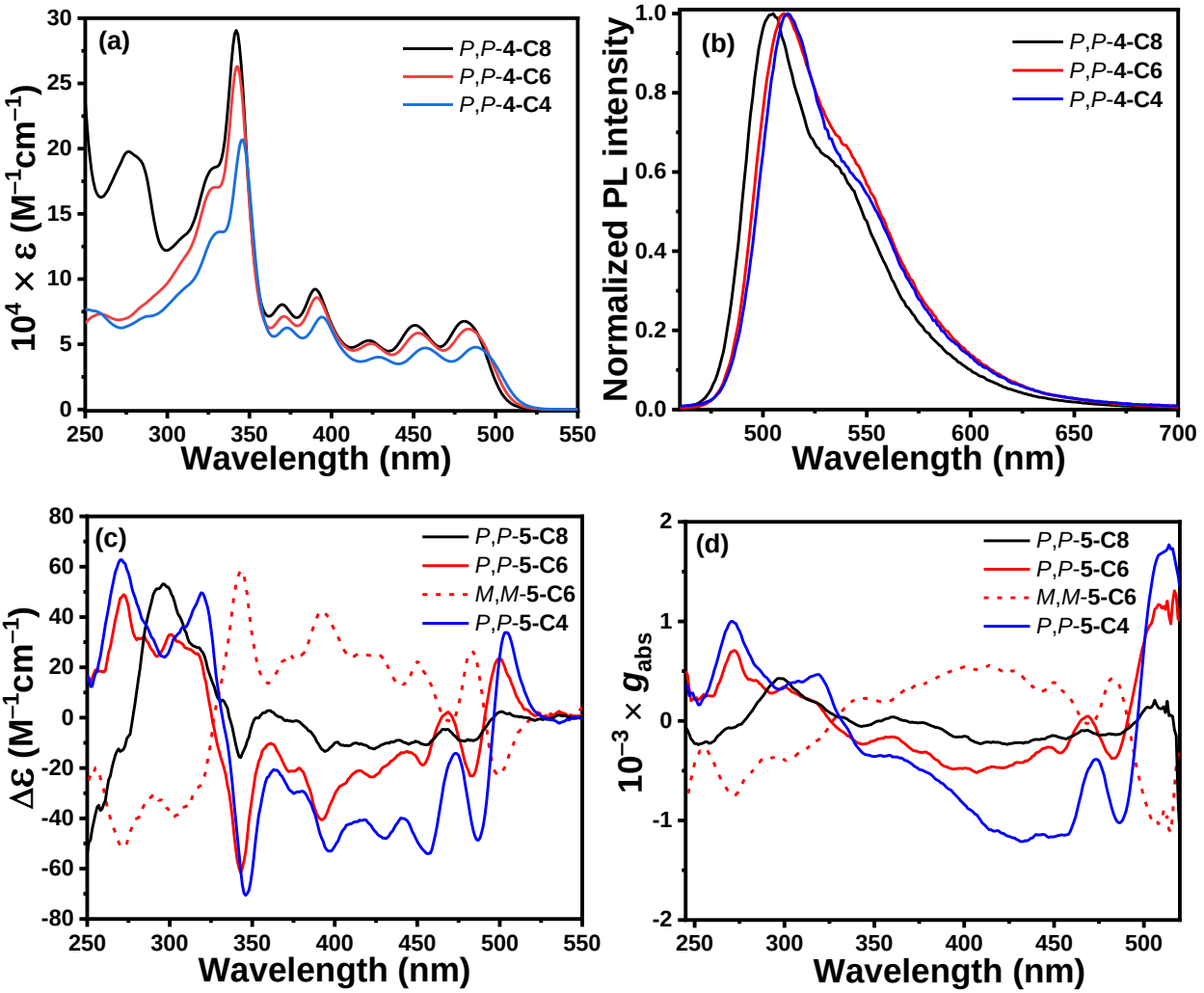

Figure S28. Photophysical and chiroptical properties of **4-Cn** in chloroform at room temperature. (a) quantitative UV-vis spectra, (b) normalized emission spectra, (c) circular dichroism spectra and (d) g_{abs} values.

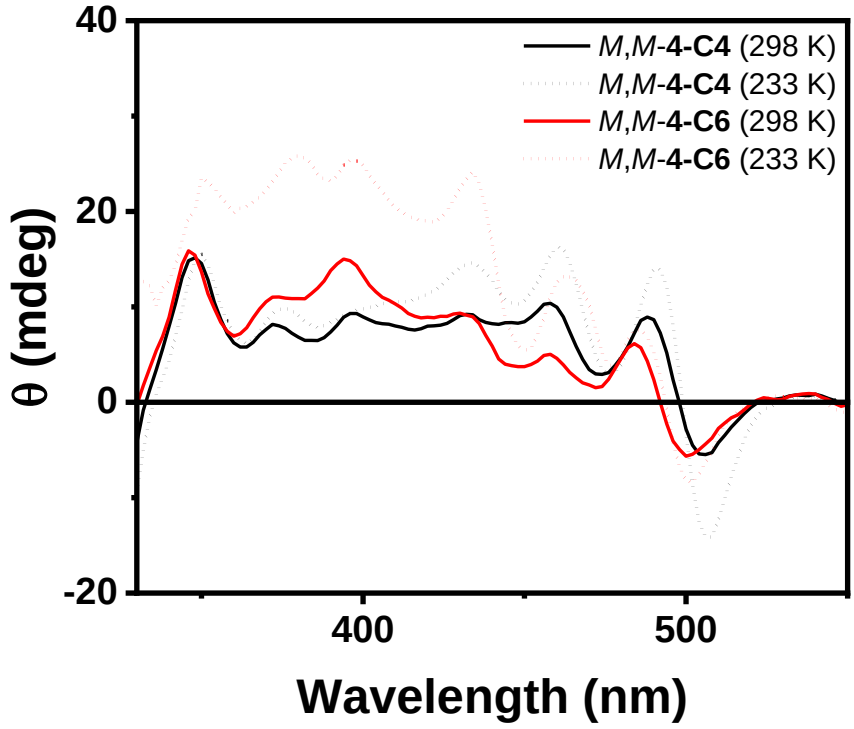

Figure S29. ECD spectra at 298K (solid) and 273K (dashed) of *M,M*-**4**-C4 (black) and *M,M*-**4**-C6 (red) in chloroform.

Brightness calculations: The brightness of 2-4-Cn was calculated according to the previously suggested formula $B = \varepsilon_\lambda \times \Phi_f \times |g_{lum}|/2$.[3] Where ε_λ is the extinction coefficient at the maxima of the lowest energy band, Φ_f is the fluorescence quantum yield and $|g_{lum}|$ is the emission anisotropy factor.

Table S1 – Photophysical properties for **2-4-Cn**.

Compound	ε_λ (M^{-1} cm^{-1})	Φ_f	$\lvert g_{lum} \rvert$	B (M^{-1} cm^{-1})
2-C4[1]	18860	0.55	0.0005	2.59
2-C6[1]	19060	0.7	0.00007	0.47
2-C8[1]	19400	0.84	0.00004	0.33
3-C3[4]	8307	0.07	0.0025	0.73
3-C4[4]	8203	0.11	0.00246	1.11
3-C5[4]	7685	0.21	0.0019	1.53
3-C6[4]	9463	0.29	0.00179	2.46
4-C4	47787	0.69	0.0008	13.19
4-C6	61687	0.82	0.0005	12.65
4-C8	67676	0.91	0.0001	3.08

S5 Computational details

All calculations were carried out using the Gaussian 09 program applying density functional theory (DFT). All molecules were optimized using a hybrid density functional[5] and Becke's three-parameter exchange functional combined with the LYP correlation functional (B3LYP)[6] and with the 6-31G(d) basis set (B3LYP/6-31G(d)). To understand the UV-vis and CD spectral transition of the molecules, time dependent (TD)-DFT calculations were performed using the CAM-B3LYP functional.

To compare the experimentally obtained optoelectronic properties of the twistacenes and their oligomers, the parent acene analogs were also examined using identical computational methods. To maintain consistency with the experimentally observed CD spectra for the synthesized molecules, which were explained by a *syn* conformation of the tethered twistacenes in oligomers, here we considered only parent oligomers in the *syn* conformation. The computational approach to twisting anthracene was as per our previously reported method.[7]

Table S2. Calculated energies of optimized structures.

	S_0 (B3LYP-6-31G(d))	**S_1 (CAM-B3LYP-6-31G(d))**
M-**Ant-10**	-846.7437762	-539.1959970
M-**Ant-20**	-846.7414347	-539.1934952
M-**Ant-30**	-846.7375167	-539.1893009
M-**Ant-40**	-846.732037	-539.1833128
M-**1C2-Ant-10**	-615.6748923	-615.2975316
M-**1C2-Ant-20**	-615.6725436	-615.2950458
M-**1C2-Ant-30**	-615.6686055	-615.2908806
M-**1C2-Ant-40**	-615.6630509	-615. 2850034
syn-*M*,*M*-**2Ant-10**	-1230.1844804	-1229.4443204
syn-*M*,*M*-**2Ant-20**	-1230.1798147	-1229.4394309
syn-*M*,*M*-**2Ant-30**	-1230.1720012	-1229.4312522
syn-*M*,*M*-**2Ant-40**	-1230.1610054	-1229.4197137

Optimized (DFT-B3LYP-6-31G(d)) geometries of the *M*-Ant-n skeletons (n = degree of end-to-end twist angle per anthracene unit)

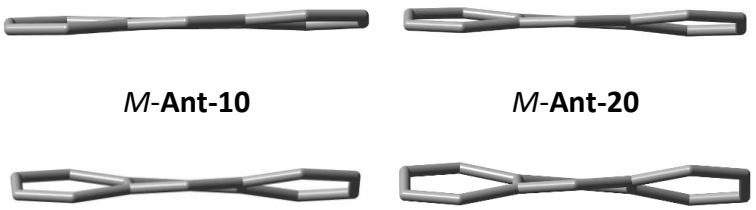

M-**Ant-10** *M*-**Ant-20**

M-**Ant-30** *M*-**Ant-40**

Optimized (DFT-B3LYP-6-31G(d)) geometries of the *M*-1C2-Ant-n skeletons (n = degree of end-to-end twist angle per anthracene unit)

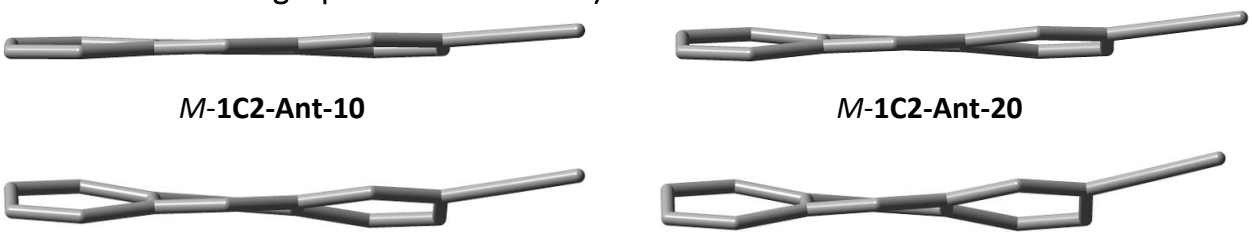

M-**1C2-Ant-10** *M*-**1C2-Ant-20**

M-**1C2-Ant-30** *M*-**1C2-Ant-40**

Optimized (DFT-B3LYP-6-31G(d)) geometries of the *M*-2C2-2Ant-n skeletons (n = degree of end-to-end twist angle per anthracene unit)

M-**2C2-2Ant-10**

M-**2C2-2Ant-20**

M-**2C2-2Ant-30**

M-**2C2-2Ant-40**

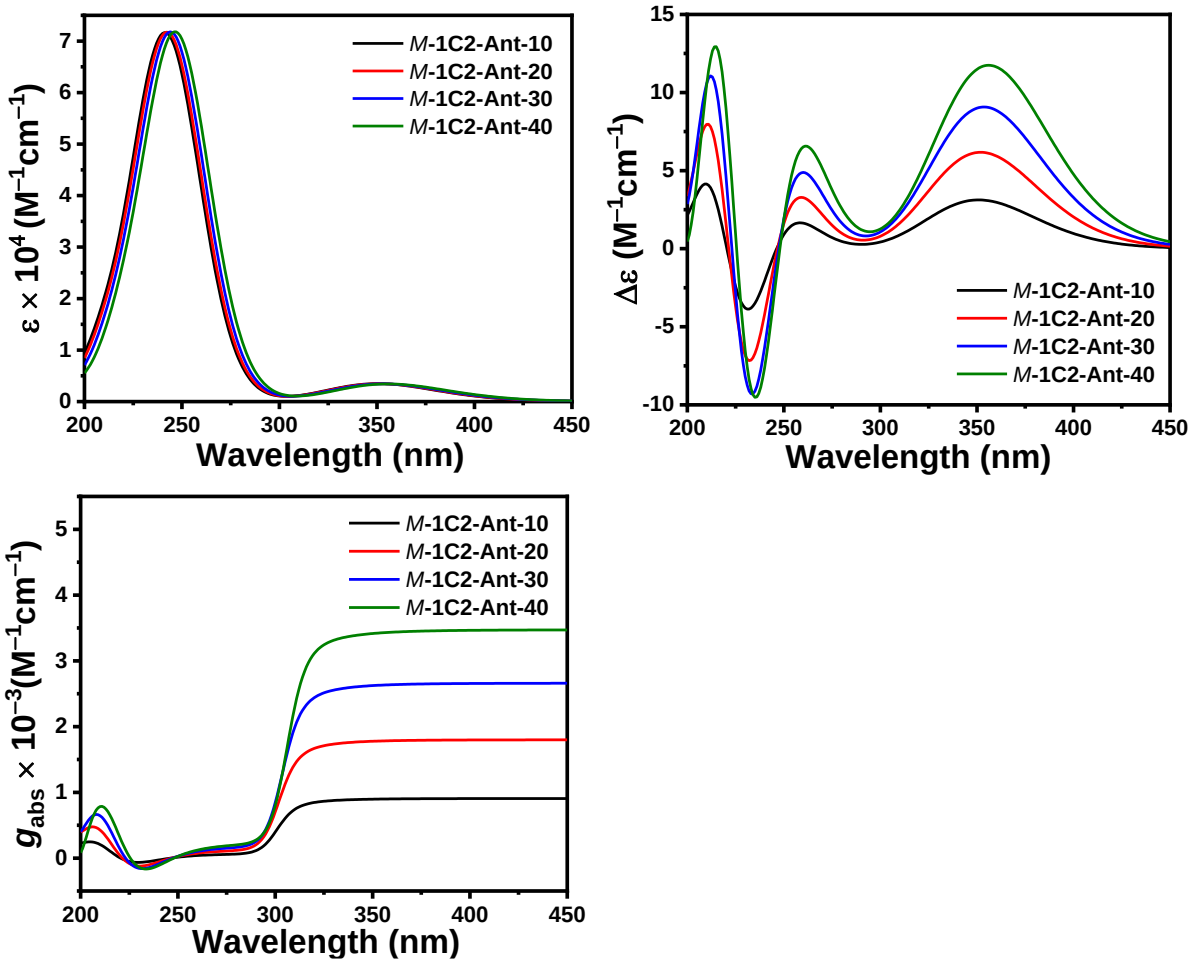

Figure S30. Calculated (a) UV-vis, (b) CD spectra and (c) absorption dissymmetry factor (g_{abs}) for *M*-1-**C2-Ant-n** skeletons.

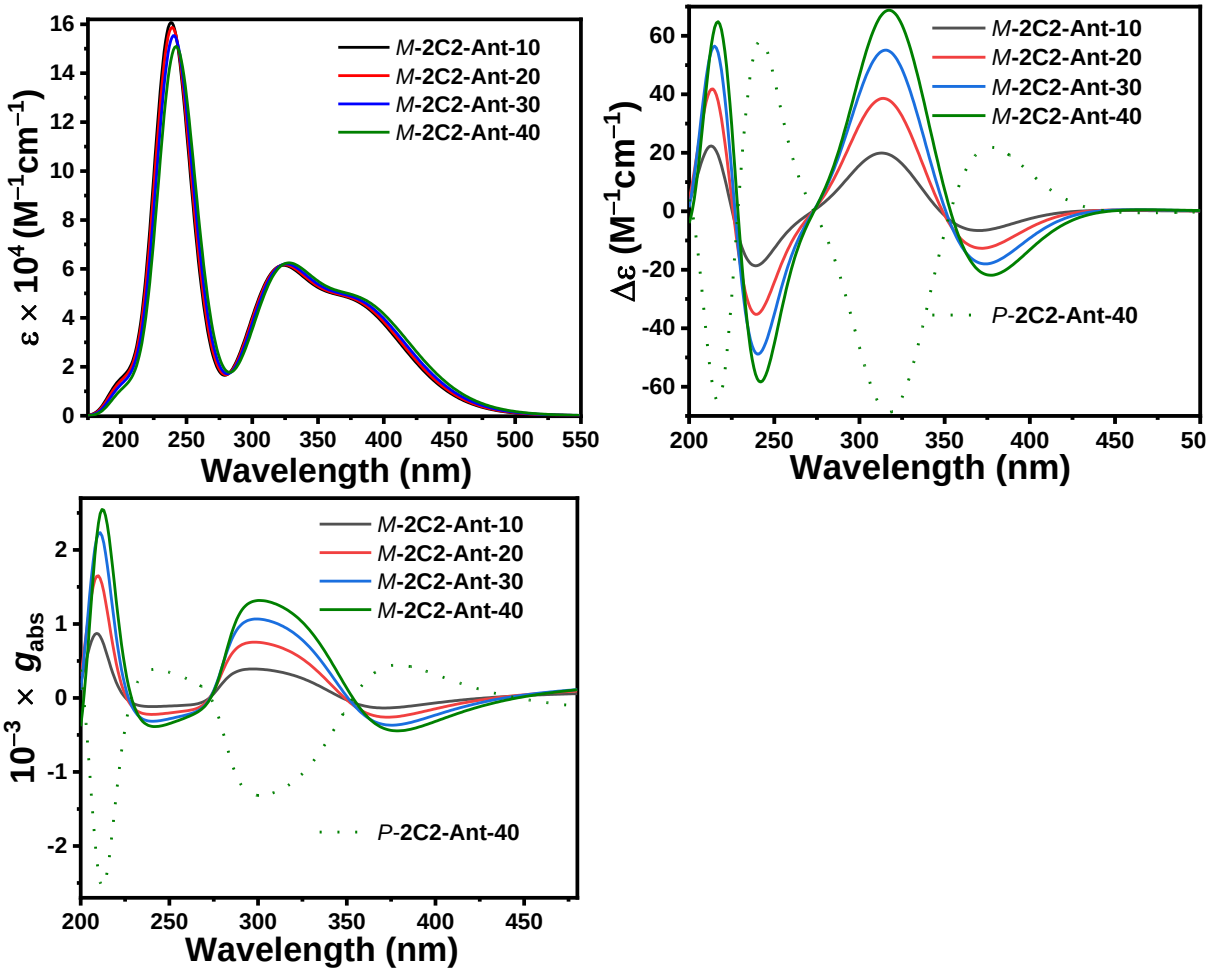

Figure S31. Calculated (a) UV-vis, (b) CD spectra and (c) absorption dissymmetry factor (g_{abs}) for *M*-2**C2-2Ant-n** skeletons.

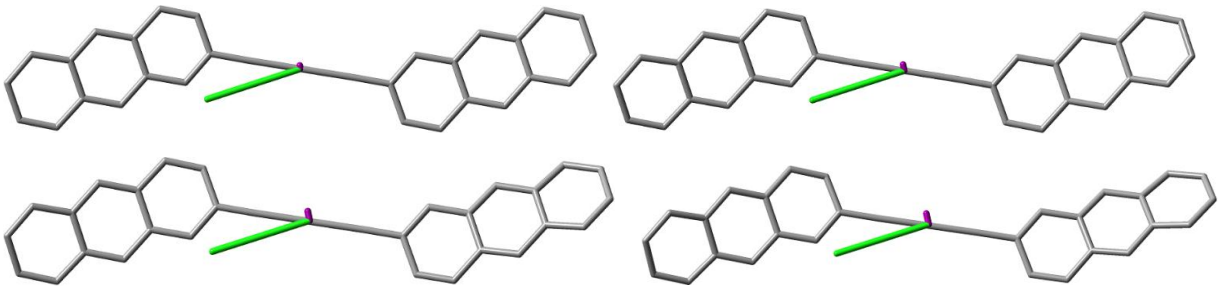

Figure S32. Calculated (DFT-B3LYP-6-31G(d)) electric and magnetic transition dipole moments of the skeletons of (a) *M*,*M*-**2-Ant-10**, (b) *M*,*M*-**3-Ant-20**, (c) *M*,*M*-**2-Ant-30** and (d) *M*,*M*-**2-Ant-40**.

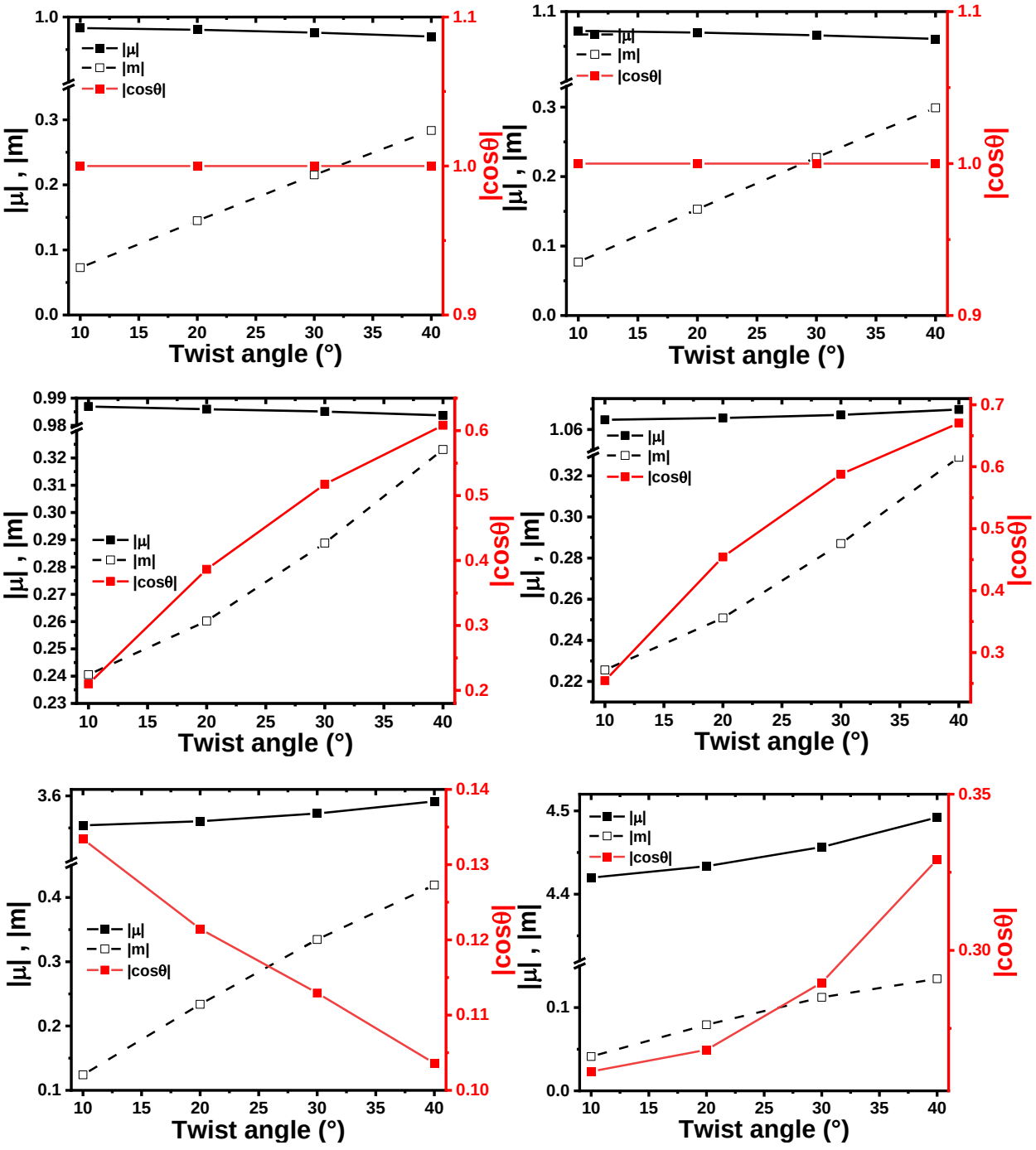

Figure S33. Computed (TDDFT-CAMB3LYP-6-31G(d)) transition dipole moments (left axis) and the rotational strength (R) and cos(θ) (right axis) at the optimized (a) S_0 of **Ant-n**, (b) S_1 of **Ant-n**, (c) S_0 of **1C2-Ant-n**, (d) S_1 of **1C2-Ant-n**, (e) S_0 of **2C2-2Ant-n** and (f) S_1 of **2C2-2Ant-n**.

References

[1] Bedi, A.; Manor Armon, A.; Diskin-Posner, Y.; Bogosalvsky, B.; Gidron, O.; *Nat. Commun.*, **2022**, *13*, 451.

[2] Hananel, U.; Ben-Moshe, A.; Diamant, H.; Markovich, G. *Proc. Natl. Acad. Sci.* USA **2019**, *116*, 11159.

[3] Arrico, L.; Bari, L. D.; Zinna, F., *Chem. Eur. J.*, **2020**, *27*, 2920.

[4] Bedi, A.; Shimon, L. J. W.; Gidron, O.; J. Am. Chem. Soc., 2018, 140, 8086.

[5] (a) Parr, R. G.; Yang, W. Density-functional Theory of Atoms and Molecules, Oxford University Press, New York, **1989**. (b) Koch, W.; Holthausen, M. C. A Chemist's Guide to Density Functional Theory, Wiley-VCH, New York, **2000**.

[6] Lee, C.; Yang, W.; Parr, R. G. *Phys. Rev. B* **1988**, *37*, 785. (b) Becke, A. D. *J. Chem. Phys.* **1993**, *98*, 5648.

[7] Bedi, A.; Gidron, O., *Chem. Eur. J.*, **2019**, *25*, 3279.